Theoretical Prediction of Sauter Mean Diameter for Pressure-Swirl Atomizers through Integral Conservation Methods

by

Ali Moradi

A Thesis Presented in Partial Fulfillment
of the Requirements for the Degree
Master of Science

Approved July 2013 by the
Graduate Supervisory Committee:

Taewoo Lee, Chair
Marcus Herrmann
Huei-Ping Huang

ARIZONA STATE UNIVERSITY

August 2013

ABSTRACT

A new theoretical model was developed utilizing energy conservation methods in order to determine the fully-atomized cross-sectional Sauter mean diameters of pressure-swirl atomizers. A detailed boundary-layer assessment led to the development of a new viscous dissipation model for droplets in the spray. Integral momentum methods were also used to determine the complete velocity history of the droplets and entrained gas in the spray. The model was extensively validated through comparison with experiment and it was found that the model could predict the correct droplet size with high accuracy for a wide range of operating conditions. Based on detailed analysis, it was found that the energy model has a tendency to overestimate the droplet diameters for very low injection velocities, Weber numbers, and cone angles. A full parametric study was also performed in order to unveil some underlying behavior of pressure-swirl atomizers. It was found that at high injection velocities, the kinetic energy in the spray is significantly larger than the surface tension energy, therefore, efforts into improving atomization quality by changing the liquid's surface tension may not be the most productive. From the parametric studies it was also shown how the Sauter mean diameter and entrained velocities vary with increasing ambient gas density. Overall, the present energy model has the potential to provide quick and reasonably accurate solutions for a wide range of operating conditions enabling the user to determine how different injection parameters affect the spray quality.

ACKNOWLEDGMENTS

This author would like to thank Dr. Taewoo Lee for his advice on developing the model. This author would also like to thank Dr. Marcus Hermmann for his valuable advice on the development of the viscous dissipation model.

TABLE OF CONTENTS

Page

LIST OF FIGURES

CHAPTER 1

INTRODUCTION

I. Introduction:

Throughout the past century atomizers have been used in a myriad of engineering applications ranging from pharmaceutical applications to spraying of crops with water and chemicals in the agricultural field. Atomizers also have a direct function in various combustion applications such as fuel injection in gas turbine engines, diesel engines, rockets, and in industrial furnace burners. In addition to simply supplying fuel to the combustor, they have numerous other functions that they must satisfy in order to aid in the combustion process. It has been well documented that normal liquid fuels used in modern burners lack the appropriate volatility to generate enough vapor to begin ignition and feed combustion and must therefore be atomized into sufficiently small droplets to increase the total surface area of the liquid, thereby increasing the evaporation and mixing rates (Lefebvre, *Atom. & Sprays*; Lefebvre, *Gas Turb. Comb.*; Mellor). Atomizers are also known to affect combustion stability limits, combustion efficiency, smoke generation, and carbon monoxide and unburned hydrocarbon levels (Lefebvre, *Gas Turb. Comb.*). In general, reduction in the droplet size will increase volumetric heat release rates, lower exhaust concentrations of pollutants, allow for a much more manageable light-up process, and enable for a wider range of burning conditions (Lefebvre, *Atom. & Sprays*).

Atomizers are also used to distribute drops in the primary zone of the combustor to control mixture distribution and facilitate rapid mixing. The proper distributions are achieved through fuel spray penetration and aerodynamic flow patterns in the combustor

(Mellor). Fuel penetration and spray angle are also known to affect exhaust smoke (Lefebvre, “Fact. Cont. Gas. Turb.”). This occurs due to the fact that smoke is generally created in fuel-rich locations in the flame-tube near the atomizer; therefore, using a proper cone angle and improving fuel penetration will reduce the generation of smoke by reducing excess fuel concentrations in that region (Lefebvre, “Fact. Cont. Gas. Turb.”). In addition to the previously mentioned functions, it should be noted that modern day combustors operate at very high compression ratios and experimental evidence has shown that combustion efficiency becomes less dependent on reaction rates and more on evaporation and mixing rates, making atomization quality of critical importance at high compression ratios (Lefebvre, “Fact. Cont. Gas. Turb.”).

Injectors are designed in a variety of different forms; however, the general mechanism in the atomization process is to utilize the kinetic energy of the fuel (or the kinetic energy of the gaseous medium for air-assisted atomizers) to increase the total surface area of the fuel. Each individual type of injector achieves this through its own unique way which has specific advantages and disadvantages. The two most common types of injectors are pressure atomizers and air-assisted atomizers. Pressure atomizers utilize high injection pressures to discharge fuel from a relatively small orifice. The total pressure head inside the injector is converted into kinetic energy and used to break down the bulk fuel into small droplets. Pressure atomizers come in numerous subcategories; plain-orifice injector, pressure-swirl injector, duplex injector, dual orifice injector, and many other similar forms.

Plain-orifice injectors are one of the simplest forms of pressure atomizers. In general, a small circular orifice is utilized to inject the fuel under high pressure as a round

liquid jet. This jet will then breakdown due to instabilities and aerodynamic interactions into numerous small droplets. Droplets produced by plain-orifice atomizers generally scale with the injector diameter, therefore decreasing the orifice will result in smaller droplets. While this can be beneficial for combustion applications, the injector diameter is usually limited due to clogging of foreign particles in the fuel (Lefebvre, *Atom. & Sprays*). Plain-orifice injectors are extremely simple and durable, making them ideal for turbojet afterburners, ramjets, and diesel and rocket engines (Lefebvre, *Atom. & Sprays*). They are limited by their small cone angles (5°-15°) and their poor capability of distributing fuel within the combustor (due to the solid cone nature of the spray pattern) (Lefebvre, *Atom. & Sprays*). These limitations make the plain-orifice atomizer a poor choice for high-performance machines such as gas-turbine engines. To circumvent these issues, a swirl component may be added to increase the cone angle and give better fuel distribution. This is the main function of the pressure-swirl atomizer.

In a pressure-swirl (simplex) injector, liquid flows through a number of tangential holes or slots into a swirl chamber. The swirling liquid will generate a core filled with the gaseous medium that extends from the injector orifice to the swirl chamber effectively creating a thin sheet of liquid near the injector walls. The hydrodynamics of the swirl atomizer can be relatively complex as it has theoretically and experimentally been shown that the majority of fluid flows through the boundary layer developed within the nozzle, and that perfect fluid theory can generate erroneous results if applied within the atomizer (Taylor, “Mech. Swirl Atom.”; Binnie and Harris). In the swirl chamber, a portion of the swirl energy will be converted into axial velocity and the liquid will flow out of the nozzle in the form of a hollow cone. Solid-cone pressure-swirl atomizers can also be

designed by injecting liquid in the center of the cone. Due to the high swirl velocities, simplex injectors can usually achieve very high cone angle (30°-180°) which gives them tremendous atomization performance. In addition, the various range of cone angles exhibited by these injectors gives them good fuel distribution performance (Lefebvre, *Atom. & Sprays*). Due to the extra swirl energy and relatively high cone angles, the droplets in pressure-swirl atomizers tend to be much smaller than the plain-orifice atomizer. Owing to their relatively high performance, pressure-swirl atomizers are generally used inside gas turbine engines and industrial sized burners (Lefebvre, *Atom. & Sprays*). The greatest disadvantage of these injectors is that they require very high injection pressures and that their cone angle varies with operating conditions such as the injection pressure and the ambient density of the gas (Lefebvre, *Atom. & Sprays*). In addition, simplex nozzles tend to have low discharge coefficients due to the air core that covers the majority of the injector orifice. These issues can be ameliorated by utilizing multiple liquid supply lines such as in the case of duplex atomizers. While there are numerous other injector types such as air-assisted atomizers, the present study will focus on pressure-swirl injectors because of their high performance and wide range of applicability.

The injector design is not the only factor that governs atomization performance; liquid properties and ambient gas properties can significantly alter the mean droplet size and distribution. The liquid surface tension and viscosity tend to prevent breakup and instabilities, whereas the gas density will promote instability and breakup due to aerodynamic interaction. Liquid density, while having a smaller overall effect on the flow, can also alter performance as the higher inertia of the liquid phase can be less

susceptible to the aerodynamic effects of the gaseous medium. This can be shown theoretically by observing the boundary conditions at the material interphase (Batchelor). In addition to fluid properties, different instability mechanisms are paramount to the atomization process. These instability mechanisms include the Kelvin-Helmholtz instability arising from the interfacial shear across the liquid-gaseous boundary, and the Rayleigh-Taylor instability that forms due to the different densities of the two fluids. While these instability mechanisms are prevalent mostly in the primary atomization process, they are still significant in the secondary atomization regime (Guildenbecher et al.; Theofanis et al.). Droplet and entrained air turbulence is also a major performance-altering factor as it can affect the liquid distribution and droplet sizes of the spray (Rosa et al.). It has been shown experimentally that droplet-droplet interactions such as coalescence can significantly alter the mean droplet size and distribution (Saha et al.). Finally, it is imperative to note that instabilities within the internal sections of the atomizer can affect the flow indirectly. These instabilities can result from fluctuating pressure supplies or liquid cavitation within the nozzle.

Owing to these highly coupled and competing phenomena, liquid atomization physics tends to be highly complex in nature. Various investigations have been proposed and conducted with varying degrees of success in order to relate the injector geometry and fluid properties to the necessary atomization parameters such as mean droplet size, droplet velocity, droplet distribution, spray cone angle, entrained air, and the spray penetration depth. These investigations include experimental, numerical, and theoretical work.

II. Empirical Investigations:

Numerous experiments to predict the Sauter mean diameter (SMD) of a pressure-atomized spray have been performed in order to determine a functional relationship between the SMD and the relative parameters such as surface tension, viscosity, and liquid and gas densities (see Lefebvre, "Pred. Saut. Mean Diam." for review). Wang and Lefebvre conducted an experiment in which they utilized two pressure-swirl atomizers with different flow numbers to determine the proportionality of the SMD with the surface tension of the liquid. They discovered that SMD scales proportional to $\sigma^{0.25}$ (Lefebvre, "Pred. Saut. Mean Diam."). Similar results were found by Jones and Simmons and Harding (Lefebvre, "Pred. Saut. Mean Diam.") with slight variation in the constant power. In addition, various published data seem to indicate that, on average, SMD scales proportionally to $\mu_L^{0.16}$ with slight variations between the different experiments (Lefebvre, "Pred. Saut. Mean Diam.").

Saha *et al.* attempted to quantify the average droplet diameters and velocities due to the breakup and subsequent coalescence of the droplets from two different simplex atomizers utilizing PDPA and shadowgraph techniques. They discovered that regardless of the injector diameter used, the droplet diameters and velocities all converged to the same value at axial distances far from the injector orifice. The final droplet velocities seem to only vary with respect to the injection pressure near the nozzle; however, far enough downstream all the droplet velocities converged to the same value along the center axis. They also discovered that even though the simplex nozzles were of the hollow-cone type, they still had significant number of droplets along the center axis. This was attributed to the fact that smaller droplets are going to be carried inwards by the

entrained gas, whereas the larger droplets would continue along their path at the sheet breakup point. Finally, it should be noted that they observed appreciable coalescence effects downstream of the nozzle.

Tratnig and Brenn conducted an extensive study utilizing five different orifice diameters, four different combinations of swirl chamber widths, heights, and inlet diameters, and various liquids. These investigations combined into 30 independent experiments that they used to validate theoretical models. They used phase-Doppler anemometry and visual techniques to measure the cross-sectional SMD values, sheet breakup length, spray cone angle, and mass flow rate. They discovered that the non-dimensional SMD with respect to the swirl chamber diameter scales according to $Re_p^{-0.8505}$ and $Oh^{-0.7538}$, where Re_p and Oh are the pressure-based Reynolds number and the Ohnesorge number, respectively. They attempted to use their results to validate the Dombrowski and Johns linear stability model (Dombrowski and Johns), but it was found that the model tends to highly overestimate the sheet breakup length.

It is well known that once the initial conical sheet breaks up, the droplets entrain a significant amount of air (or other gaseous media) inside the spray zone. This occurs due to a momentum exchange between the droplets and the surrounding medium (Rothe and Block). Prosperi *et al.* attempted to quantify this entrained gaseous velocity through particle image velocimetry (PIV) with fluorescent tracers. They showed that the entrained air enters normal to the sheet angle at breakup and there is very little velocity component tangential to the conical spray volume. They conducted their experiments for ambient densities ranging from 1.2 kg/m^3 to 18 kg/m^3. They found that the entrained mass flow rate increased significantly as the air density was increased.

While experimental work is essential for development of atomization theory, the results are only valid within the operating conditions of the experiment. Due to the fact that the flow is extremely complex and its governing parameters are highly coupled, extrapolation of results can be dangerous and misleading. One method of mitigating this issue is to perform numerical simulations for a much wider range of operating conditions.

III. Numerical Investigations:

Various types of numerical experiments have been performed over the past few decades for pressure atomizers. These studies consist of the more detailed Large Eddy Simulations (LES) of Herrmann (Herrmann) to the various boundary element methods and phenomenological numerical simulations. For a detailed review of the various Direct Numerical Simulations (DNS) and phenomenological simulations, see Gorokhovski and Herrmann. Full DNS simulations are extremely beneficial as they reveal certain flow physics that are practically invisible to experiments due to limitation in instrumentation; however, these simulations are often costly and require significant resolution in order to resolve all the length scales of the flow. In addition to the normal numerical considerations, careful attention must be paid to tracking the interfacial boundary and all the surface tension forces. These difficulties can be circumvented at high computational cost which generally limits the operating conditions of the simulations.

Park and Heister developed an axisymmetric boundary element method that simulates the atomization process of a pressure-swirl atomizers for low viscosity liquids. They used the classical results of Ponstein to determine the satellite droplet sizes. Their

simulations took over 15 days to complete on high performance computer clusters. They found that their prediction for the SMD was, in general, 30-40% smaller than experiment.

Due to the significant computational costs and time constraints mentioned previously, it is imperative that theoretical models be developed alongside numerical and experimental work. These models can then be employed in parametric studies or as a means to provide initial conditions for CFD analysis.

IV. Theoretical Investigations:

The majority of theoretical models developed for predicting the droplet diameters are based upon linear instability analysis of the primary atomization regime. These methods analyze the growth of infinitesimally small perturbations in the fluid and try to predict the correlation between the most unstable wave and the corresponding ligament diameters. Conservation of energy and mass is then applied to determine the droplets produced from the unstable ligament. A full detailed account of theoretical advancements in primary atomization is given by Lin and Reitz. One of the most quoted and studied linear stability analyses of sheet disintegration is by Dombrowski and Johns where they analyzed the disintegration of a liquid sheet of varying thickness (Dombrowski and Johns). Their results were successful when compared to experiment for the majority of the cases; however, it was discovered that the theoretical model had difficulty predicting the smaller diameters accurately. There have been many variations of the work done by Dombrowski and Johns. Unfortunately, the majority of these models predict droplets that are formed immediately following primary atomization and cannot accurately predict the final atomized mean droplet size.

Significant theoretical work has been done in determining the droplet velocity history and entrained airflow (see Rothe and Block; Cossali; Lee and Tankin, “Stud. Liq. Spray Non-cond.” and “Stud. Liq. Spray Cond.”; Ghosh and Hunt). The droplet velocity and entrained air are coupled through the momentum exchanges between them. In general, most theoretical models are one dimensional in nature and assume a constant representative diameter and droplet distribution derived from experiment in order to calculate the droplet velocity change. While these models work well and aid in understanding of the underlying physics, they are, in general, too dependent upon experimental parameters to make them of any practical value.

Rothe and Blocke derived a highly simplified model for determining the magnitude of the entrained airflow and droplet velocity. They assumed that the entrained gas enters the control volume perpendicular to the initial cone angle and instantaneously turns into the axial direction. Based on this, they used a combined liquid-gas momentum balance to determine the velocity change of the droplets. They had limited success in calculating the entrained velocity in a small range of operating conditions.

Another 1-D analysis was performed by Ghosh and Hunt where they assumed that the flow is droplet driven and the only acting force is the drag on the droplets. Utilizing the mass balance to calculate the liquid void fraction and some turbulence models, Ghosh and Hunt were able to determine the momentum imparted onto the air at various axial locations downstream of the nozzle. Their results seemed to follow experiment fairly closely indicating that this may be the correct method for calculating the induced air flow. With that in mind, it is important to note that the turbulent models and constants used in their study were not developed for multiphase jets and that there were some *ad*

hoc assumptions made in regards to the entrained length scales. As such, there is need to develop a more detailed model that does not rely on such assumptions. It is also imperative that a value for the representative diameter be derived from first principles so as to minimize the empirical dependencies of the model.

Cossali developed a 1-D integral model for gas entrainment in full cone sprays. This model assumed that the flow is self-similar and droplet driven. While this assumption is not exactly accurate near the nozzle, experiments have shown that similar to a single-phase turbulent jet, the droplet and air flow become self-similar at sufficient distances downstream (Santolaya et al.). The result of this theoretical work was that the dependencies of the entrained mass flow rate on the distance from the nozzle are noticeably different than the much-studied steady gaseous jet. It was discovered that the mass flow rate in the near field follows a 3/2 power law, whereas far downstream it behaves linearly with respect to the axial distance similar to a gaseous jet. Finally, it is important to note that Cossali's results were dependent upon acquiring a representative diameter from experiment. The integral model developed by Cossali will be extended for hollow-cone sprays in subsequent chapters in this paper.

The previously mentioned bodies of work only accounted for the droplet portion of the spray and assumed that the conditions at the point of sheet breakup are the same as the inlet. This is not always true as the cone angle can increase appreciably during the primary atomization process. This is especially true for pressure-swirl atomizers as the swirl component of the velocity will tend to increase the cone angle due to centrifugal force. In addition, even if viscous forces are ignored in the primary atomization regime, the swirl component of velocity will still have decreased drastically at the point of

breakup due to the expanding conical sheet and the conservation of angular momentum. Lee and Tankin attempted to quantify this process by including a sheet portion to their calculations ("Stud. Liq. Spray Non-cond." and "Stud. Liq. Spray Cond."). They employed the previous work of Taylor (Taylor, "Water Bells") where he equated the forces across a portion of the sheet, assuming infinitely small sheet thickness, to determine the governing equation for the dynamics of the conical sheet. In contrast to Taylor, Lee and Tankin elected not to make any simplifying assumptions in regards to the flow variables and resorted to experimental parameters for their calculations. In addition, instead of assuming constant cross-sectional velocities for the droplet portion of the spray, they employed arbitrary velocity distributions across the cross section in order to calculate the entrained airflow. Their result correlated well with their experiment, but it was highly dependent upon experimental parameter inputs in order to complete the calculations.

As mentioned previously, the primary function of an atomizer is to utilize the kinetic energy of the liquid in order to increase the total surface area of the fluid by breaking up the bulk liquid into small droplets. With this logic, it is then natural to use energy conservation methods in order to calculate the representative droplet size. Lee and colleagues did this for plain-orifice atomizers (Lee and Robinson; Lee and Lee). They achieved this by applying the mass, momentum, and energy conservation equations to a control volume encompassing the entire spray volume (see fig. 1.). The control volume exit plane was chosen to be far enough so that both the liquid and gas phase were at an equilibrium. This effectively ensures that all the liquid has been broken down into spherical droplets and no further atomization occurs.

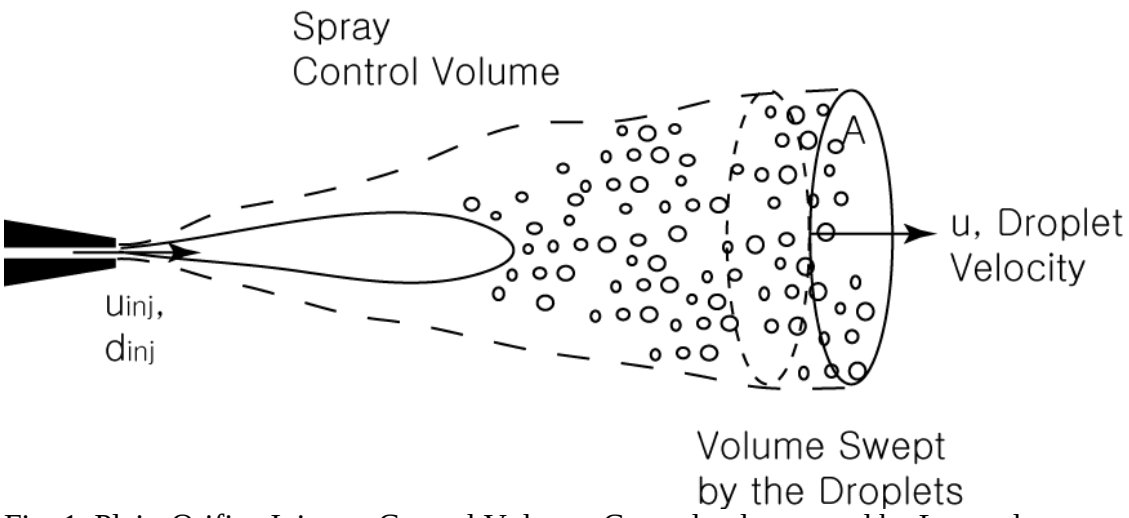

Fig. 1. Plain-Orifice Injector Control Volume. Control volume used by Lee and Robinson for calculation of droplet velocity and diameter.

They first employed the continuity equation in order to solve the droplet number density. These equations are repeated below for convenience.

$$\rho_L u_{inj} A_{inj} = \int_{u=0}^{u_{\max}} \int_{D=0}^{D_{\max}} n\bar{p}(D,u)\frac{\pi D^3}{6}\rho_L u A dD du \approx \frac{\pi}{6} n \rho_L \bar{u} A \sum_i^N p(D_i) D_i^{\,3} \Delta D_i$$

$$n = \frac{\rho_L u_{inj} A_{inj}}{\frac{\pi}{6}\rho_L \bar{u} A \sum_i^N p(D_i) D_i^{\,3} \Delta D_i}$$

In the above equations, n is the droplet number density, D_i is the droplet diameter, $P(D_i)$ is the normalized droplet size distribution, and ΔD_i is the drop size bin width. In the above formulations it was assumed that all droplets were travelling at an average cross-sectional velocity. Considering only the kinetic energy and the surface tension energy of the droplets, they were able to formulate an equation for the Sauter mean diameter (SMD). This was done by utilizing the integral form of the energy conservation equation given below

$$\rho_L \frac{u_{inj}{}^3}{2} A_{inj} = \frac{\pi}{12} n \rho_L \bar{u}^3 A \sum_i^N p(D_i) D_i{}^3 \Delta D_i + n \bar{u} A \pi \sigma \sum_i^N p(D_i) D_i{}^2 \Delta D_i$$

By substituting the droplet number density into the energy balance, an equation for the SMD can be acquired directly.

$$\frac{\sum_i^N p(D_i) D_i{}^3 \Delta D_i}{\sum_i^N p(D_i) D_i{}^2 \Delta D_i} = D_{32} = \frac{6\sigma}{\rho_L \left(\frac{u_{inj}{}^2}{2} - \frac{\bar{u}^2}{2} \right)}$$

Given the final droplet velocities, the representative droplet diameter can be easily calculated from the above equation. In order to determine the droplet velocity, Lee and Robinson applied the momentum conservation equation for the gas and liquid phase to get

$$\rho_L u_{inj}{}^2 A_{inj} = \frac{\pi}{6} n \rho_L \bar{u}^2 A \sum_i^N p(D_i) D_i{}^3 \Delta D_i + \frac{1}{2} n V_{spray} \rho_a \sum_i^N C_{Di} (\bar{u} - u_a)^2 \, p(D_i) \frac{\pi D_i{}^2}{4} \Delta D_i$$

$$\rho_a u_a{}^2 A = \frac{1}{2} n V_{spray} \rho_a \sum_i^N C_{Di} (\bar{u} - u_a)^2 \, p(D_i) \frac{\pi D_i{}^2}{4} \Delta D_i$$

Substituting the droplet number density into the above equations, the momentum equations can be written in terms of the SMD and average liquid and gas velocities.

$$\rho_L u_{inj}{}^2 A_{inj} = \rho_L \bar{u} u_{inj} A + C_D \frac{1}{2} \rho_a (\bar{u} - u_a)^2 \frac{3 u_{inj} A_{inj} V_{spray}}{2 \bar{u} A D_{32}}$$

$$\rho_a u_a{}^2 A = C_D \frac{1}{2} \rho_a (\bar{u} - u_a)^2 \frac{3 u_{inj} A_{inj} V_{spray}}{2 \bar{u} A D_{32}}$$

Here C_D is the drag coefficient and can be taken from standard empirical relationships for spheres in steady flow. Lee and Robinson elected to solve these equations iteratively where the final droplet velocity was assumed, and an SMD value was calculated from the

equation for the Sauter mean diameter. Using this SMD value, they calculated the droplet velocity from the integral momentum conservation equations and used it to update the Sauter mean diameter. This process was repeated until convergence was reached. They validated their results by comparing with experiment for various different injection pressures (see fig. 2.). The results obtained matched experiment reasonably well with the exception that the pressure dependence of the theoretical model was much steeper than the experimental evidence.

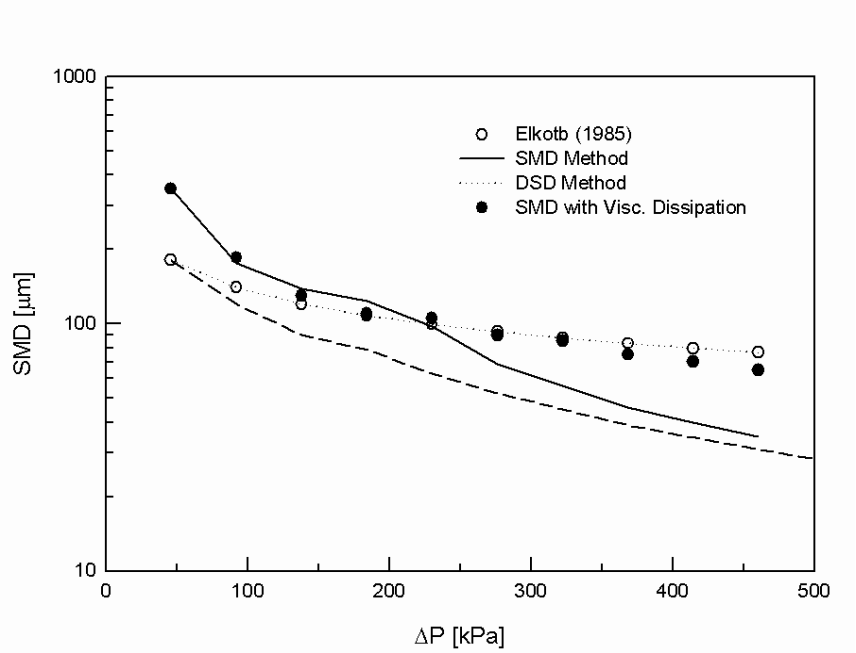

Fig. 2. SMD Variation with Injection Pressure. Results obtained by Lee and Robinson for the Sauter mean diameter.

In order to ameliorate this, they included a term that accounted for the energy dissipated due to liquid viscosity. For the dissipation term they assumed a model of the form

$$\mu_L \left(\frac{\partial u}{\partial y} \right)^2 (SprayVolume) \sim K \mu_L \frac{u_{inj}^{\ 2}}{d_{inj}^{\ 2}}$$

The constant parameter was chosen to best match experiment and was approximately on the order of 100. This improved their results (see fig. 2.), but the length and velocity scales used for the viscous dissipation term may not be appropriate. In addition to finding the SMD value, Lee and Robinson were also able to determine the droplet distributions. Assuming a log-normal distribution, the second order and third order moments can be written as

$$\left\langle D^2 \right\rangle = E(D^2) = \exp\left(2\mu + 2s^2\right)$$

$$\left\langle D^3 \right\rangle = E(D^3) = \exp\left(3\mu + \frac{9}{2}s^2\right)$$

Where μ and s are the mean and standard deviation, respectively. Lee and Robinson used these equations to find a functional relationship between the mean and standard deviation in terms of spray parameters. This relationship is given below for convenience.

$$s = \frac{2}{5}\left[\log\frac{6\sigma}{\rho_L\left(\frac{u_{inj}^{\ 2}}{2} - \frac{\overline{u}^2}{2}\right)} - \mu\right]$$

They then solved this equation iteratively using 15 different bin widths. Their results matched experiment well (see fig. 3 and 4.). Lee and Robinson did note in their paper that their solver had stabilities issues for certain injection pressures. These issues were mitigated in a follow up paper by Lee and Lee.

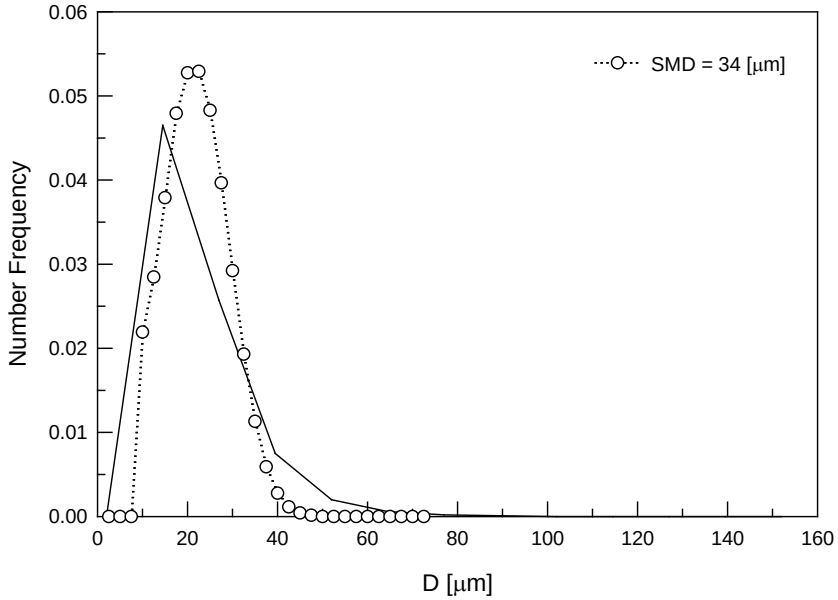

Fig. 3. Droplet Distribution for Plain-Orifice Atomizer. Droplet distribution obtained by Lee and Robinson for SMD = 34 microns.

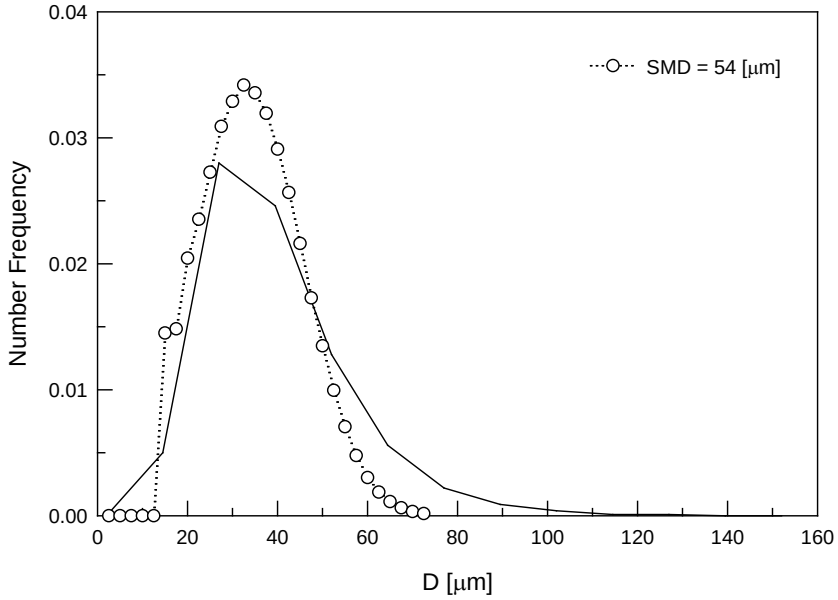

Fig. 4. Droplet Distribution for Plain-Orifice Atomizer. Droplet distribution obtained by Lee and Robinson for SMD = 54 microns.

Lee and Lee employed the previous works of Rothe and Block to perform the momentum calculations. In this method, the following two equations are used to simultaneously solve for the gas and liquid phase velocities.

$$\rho_L u_{inj} A_{inj} = \rho_L \bar{u} A + \rho_g u_g A$$

$$\frac{\pi}{6} D^3 \rho_L \bar{u} \frac{d\bar{u}}{dx} = -C_D \frac{\pi}{4} D^2 \rho_g \frac{\left(\bar{u} - u_g\right)^2}{2}$$

The benefit of using such a method is that they were able to calculate the entire velocity history of the droplets (see fig. 5.).

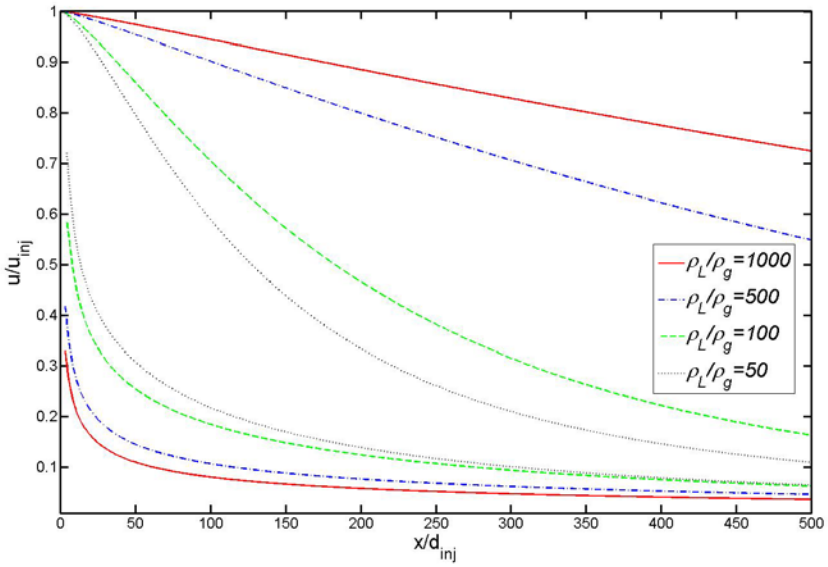

Fig. 5. Normalized Liquid and Gas Velocities for Plain-Orifice Injector. Axial variation of droplet velocity taken from the work of Lee and Lee.

They also utilized a different form for the viscous dissipation given by the following

$$\mu_L \left(\frac{\partial u}{\partial y}\right)^2 (SprayVolume) \sim K \mu_L \frac{u_{inj}^{\ 2} - \bar{u}^2}{d_s^{\ 2}} \frac{4}{3} Ax$$

Where d_s is the length scale of the viscous shear stress and was taken to be equal to the spray diameter. Repeating the same steps as before, Lee and Lee derived a new form for the Sauter mean diameter:

$$\frac{\sum_{i}^{N} p(D_i) D_i^3 \Delta D_i}{\sum_{i}^{N} p(D_i) D_i^2 \Delta D_i} = D_{32} = \frac{6\sigma}{\rho_L \left(\frac{u_{inj}^{\ 2}}{2} - \frac{\bar{u}^2}{2} \right) - \frac{4K}{3} \mu_L \frac{u_{inj}^2 - \bar{u}^2}{u_{inj}} \frac{x}{d_{inj}^2}}$$

Using the same iterative process as Lee and Robinson, they made several computations and compared them to experiment (see fig. 6.). Their results matched experiment very well at various axial and radial locations, but the constant parameter used was approximately 55,000 which indicates that the length and velocity scales used for the viscous dissipation was incorrect. Lee and Lee also performed several parametric studies to determine the behavior of plain-orifice atomizers (see fig. 7.).

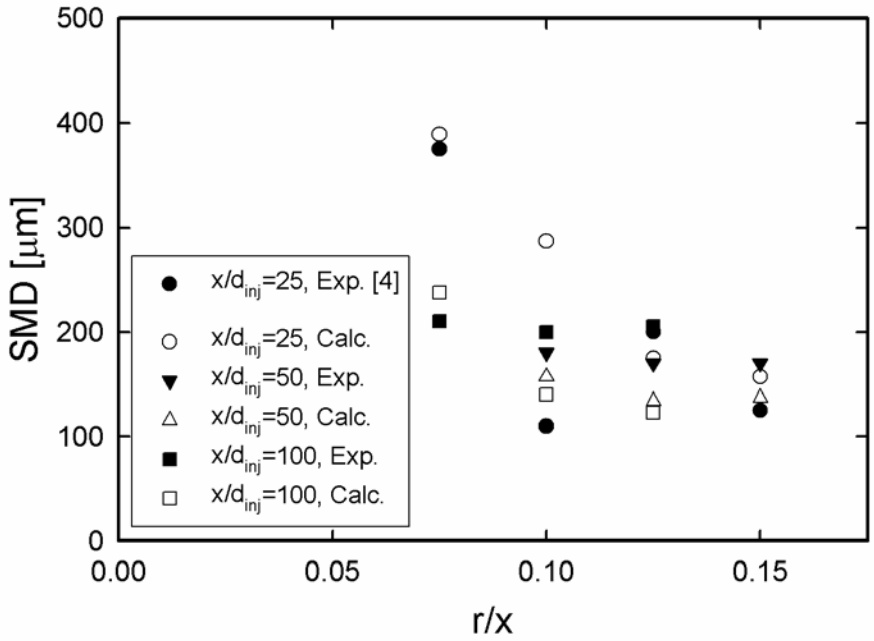

Fig. 6. SMD Calculations by Lee and Lee.

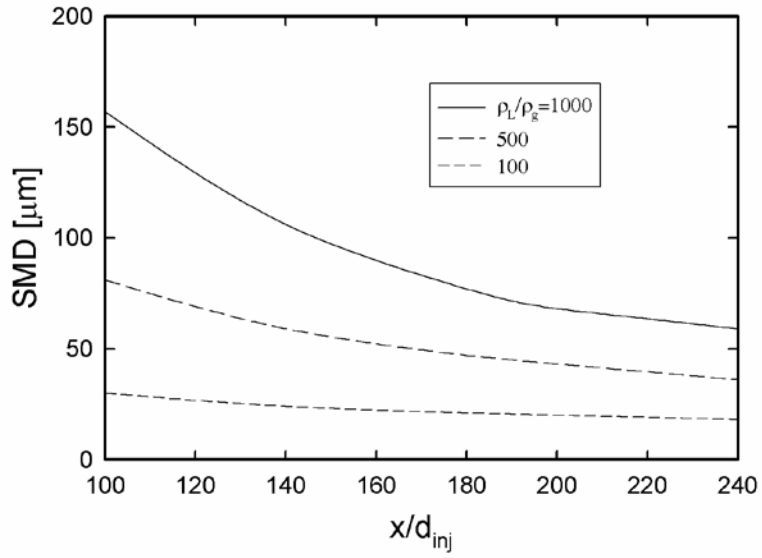

Fig. 7. Axial Variation of SMD by Lee and Lee.

In this thesis, the works of Lee and colleagues will be extended to include pressure-swirl atomizers. In addition, a new form for the viscous dissipation will be derived.

V. Objectives:

Based on the short review given of the previous bodies of work, it is evident that a new theoretical model is required that can accurately calculate the representative droplet diameters, velocities, and entrained airflow. This model should not be too dependent on experimental observations or *ad hoc* assumptions. This will be the subject of the present thesis.

The primary objective of this thesis is to derive a physically valid model to predict the cross-sectional Sauter mean diameter, the droplet velocities, and the entrained air velocities. In addition, dynamics of the conical sheet before breakup will also be included

in order to account for the variation in the liquid velocity components and the spray cone angle. The secondary goal will be to avoid having to resort to empirical parameters too often. Due to the complexities of the flow, this will not be an easy task; however, as it will be shown in later chapters, the two experimental inputs used in this paper can easily be removed with further analysis and theoretical development. The third task will be to extensively validate all aspects of the model with *independent* experiments and thoroughly explain all errors, assumptions, and shortcomings of the model. Finally, a parametric study will be performed to unveil some of the underlying physics of atomization using the current model. The aforementioned objectives will be completed in the following manner.

First, in the next chapter, a relevant physical background for pressure-swirl atomization will be given to set the stage for the derivation of the model. Next, the theoretical work of Lee and Robinson will be extended and improved upon to include pressure swirl atomizers. In addition, a more accurate viscous dissipation model will be derived based on boundary layer considerations. Next, the conical sheet dynamics will be explained based on previous work by G.I. Taylor and Bark *et al.* (Taylor, "Water Bells"; Bark et al.). Finally, the theoretical derivation by Cossali will be extended to pressure-swirl atomizers to calculate the entrained mass flow rate and droplet velocities. Once the model has been thoroughly derived and all assumptions listed, a chapter will be dedicated to validating the model with independent experiments conducted by Tratnig and Brenn, Saha *et al.*, and Prosperi *et al*. A chapter will also be dedicated to running some parametric studies with the current model and discussing the atomization behavior of

simplex nozzles. Finally, significant discussion will be made on the validity of the model, the role of the assumptions, and any improvements that can be made with future work.

CHAPTER 2

DEVELOPMENT OF MODEL

I. Theoretical Background:

Pressure-swirl atomizers differ from plain-orifice atomizers in that they have a strong tangential component of the velocity. This tangential component enables the liquid to achieve much higher cone angles as it ejects from the orifice. In addition, the liquid leaves the injector in the form of a hollow-cone spray which can drastically improve the fuel distribution in combustion applications. For the simplest form of pressure-swirl atomizers (simplex nozzle), this additional swirl component is achieved by forcing the liquid through multiple tangential slots in the injector (Rizk and Lefebvre). As the liquid enters the swirl chamber, the swirl velocity component increases due to the fact that the swirl chamber has a smaller diameter than the inlet ports. The tangential velocity also generates an air core vortex which is the main mechanism that gives the liquid its annular shape. A small portion of this swirl energy is then converted into axial velocity, and the liquid flows through a contracting nozzle. The small contraction aids in increasing the swirl component due to conservation of angular momentum, where the tangential velocity is usually assumed to be in the form of a free vortex given by the following equation.

$$U_\theta = \frac{\Omega}{r} \tag{1}$$

Where Ω is generally a function of the tangential inlet ports and r is the radius of the cross-section. In the early developments of the internal geometry of pressure-swirl atomizers, perfect fluid theory was generally assumed. Unfortunately, this usually led to erroneous results that did not match well with experimental observations. G.I. Taylor

performed boundary layer analysis using the Pohlhausen's approximation to show that the boundary layer thickness is on the same order as the annulus making irrotational flow a poor assumption in swirl injectors (Taylor, "Mech. Swirl. Atom."). Although the calculation of the flow within the nozzle is critical for determining parameters such as injection velocity, discharge coefficient, initial sheet thickness, and cone angle, this portion of pressure-swirl atomizers will be decoupled from the present problem and those parameters will be assumed as given initial conditions. Obviously the present work can always be extended to include internal geometry effects. For the cases where these parameters were not given, they were calculated in a systematic manner as will be discussed in future sections.

Once the liquid exits the injector orifice, it begins to rapidly expand into a thin conical sheet. This expansion occurs due to conservation of angular momentum, centrifugal force, and other inertial forces. The general function of the surface tension is to resist this expansion and contract the sheet inwards. This rapid expansion induces a strong radial component of velocity just outside the nozzle. This is in contrast to the internal portion of the injector where, in general, the radial component of velocity is small and may be neglected. In addition to these dynamical considerations, the difference in the velocities of the gaseous and liquid phase create a shear layer across the fluid sheet. This shear layer induces the onset of Kelvin-Helmholtz instability. Due to the fact that both phases have significantly different densities, the Rayleigh-Taylor instability is also present in the primary atomization regime. These instabilities generate waves that grow until reaching a critical amplitude at which time fragments of the liquid are broken off from the main conical sheet. These fragments will become highly unstable as they

contract under surface tension forces and eventually breakup into droplets of varying diameter (Dombrowski and Johns). In the present paper, neither of these instability mechanisms will be considered; however, detailed analysis of the dynamical behavior of the conical sheet will be made in order to determine the instantaneous cone angle of the sheet. In addition, the droplets will be assumed to be traveling at exactly the same speed as the sheet at the point of breakup. This is a fairly reasonable assumption as the droplet will not have had enough time to be influenced by aerodynamic effects.

Once the droplets break off, they will continue along their path until the aerodynamic forces carries them inwards. Usually the larger droplets will maintain their path while the smaller sized classes will be displaced towards the center axis (Saha et al.). Due to the fact that the liquid droplets deform, the aerodynamic interaction between droplets and the gaseous medium is a highly non-linear and extremely complex phenomenon. Under such aerodynamic loading, the droplets will break up further into smaller diameters. This process is generally labeled as secondary atomization. Previous work in this field generally consist of phenomenological studies such as analyzing bag breakup mode, multimode, or sheet thinning mode of droplet breakup. These different modes are highly dependent upon the droplet Weber number given by the following equation.

$$We_D = \frac{\rho_g U_R D}{\sigma} \tag{2}$$

Where U_R is the total relative velocity and D is the droplet diameter. A thorough review of secondary atomization is given by Guildenbecher *et al*. While no further consideration will be made to secondary atomization behavior, it is important to note that

the droplet diameter will not remain constant throughout this process. In addition, due to the fact that the liquid will deform under aerodynamic loading and that the droplets have a tendency to form groups, the empirical drag coefficient given for a single solid sphere is not strictly accurate. These assumptions will still be made in the present analysis, and their effect on the final results will be discussed in detail in later sections.

Experiments have shown that once secondary atomization is complete, droplet collision probability increases significantly (Saha et al.; Jiang et al.; Qian and Law). These collisions can lead to droplets bouncing off one another and exchanging momentum or to the coalescence and creation of a larger droplet. Qian and Law have shown that coalescence is dependent on the rate of dissipation of the kinetic energy of the two droplets during collision (Qian and Law; Saha et al). This probability can be quantified through a critical collision Weber number given by

$$We_{crit} = 30 * Oh_c + 15 \tag{3}$$

Where Oh_c is the collision Ohnesorge number given by the following

$$Oh_c = \frac{16\mu_L}{\sqrt{\rho_L \sigma D}} \tag{4}$$

If the collision Weber number defined by

$$We_c = \frac{\rho_L U_R D}{\sigma} \tag{5}$$

is less than the critical Weber number, then the droplets will coalesce (Saha et al.; Qian and Law). While no effort will be taken to include droplet collision in this model, the effect of neglecting such a phenomenon will be discussed in detail in the validation section.

Finally, it is critical to make a few notes in regards to the air entrainment after the initial sheet breakup. In general, in stagnant conditions, air entrainment is droplet driven and is caused by the momentum exchange between all the droplets and the gaseous medium. This flow is generally turbulent, though no account for turbulence will be made in this paper. The gaseous medium will enter the conical volume normal to a line defined by the cone angle at the sheet breakup point (see fig. 8.). At the point of breakup, the majority of the droplets will be concentrated at the outer periphery of the spray; however, the airflow will drag smaller droplets inwards towards the center axis. For the present analysis, this initial concentration of droplets at the outer edges will not be accounted for and a normal distribution will be assumed. The entrained mass flow rate is highly dependent upon the gas-liquid density ratio. As the gas density is increased, the entrained mass flow rate increases drastically. This dependence exists because there is greater momentum exchange for higher gas densities (or higher pressure, if temperature is kept constant).

Now that the physical groundwork has been laid, a formal analysis of the problem can be conducted. In the next section the governing equations for pressure-swirl atomizers will be derived in detail and all underlying assumptions will be stated explicitly.

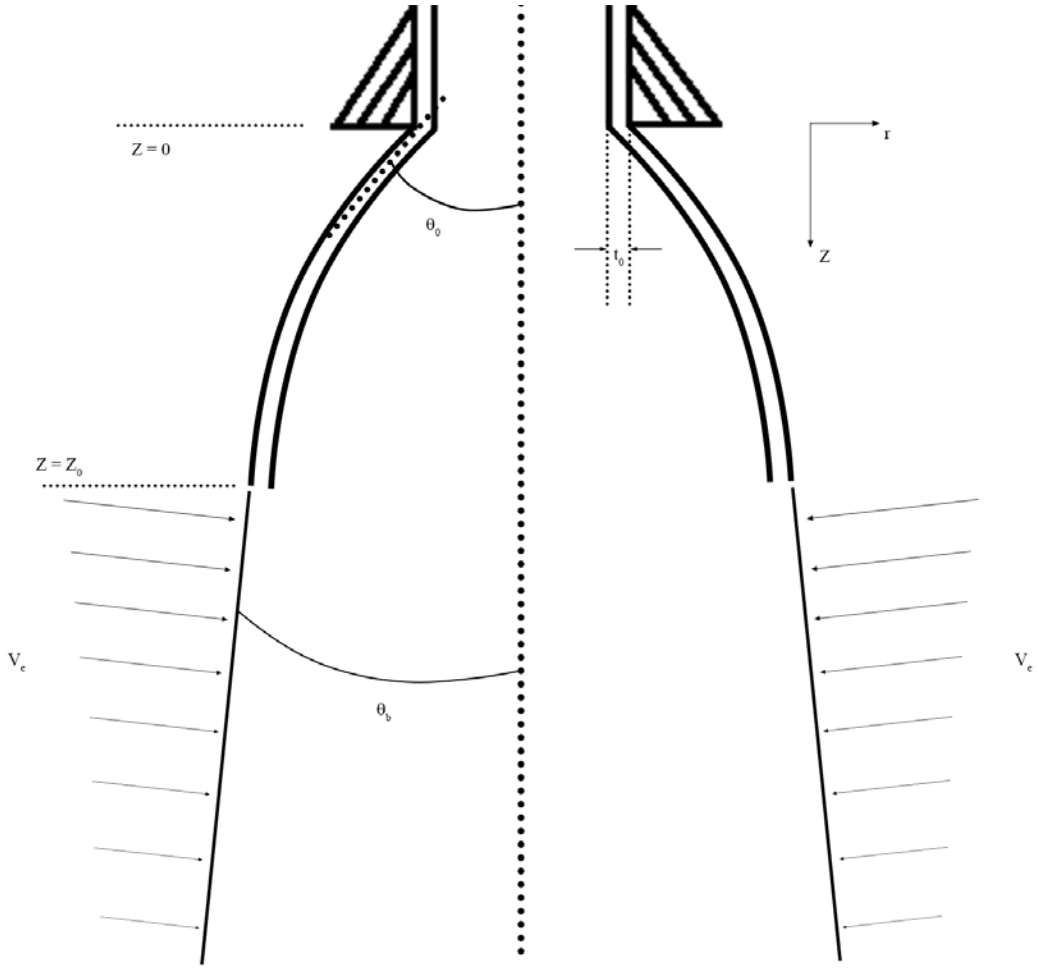

Fig. 8. Pressure-swirl Atomizer Model Diagram. Diagram depicting all relevant parameters and how the atomization process will be broken down for the present model.

II. Problem Formulation:

For the present analysis, the problem will be broken down into two sections (see fig. 8.). The first section will be the primary atomization portion defined from the injector inlet at $z = 0$ to the point where the sheet breaks apart at $z = Z_0$, where z is defined as positive along the center axis. The second portion of the problem will be the droplet section where the velocities for the droplets and entrained air are calculated. In this section, the control volume is defined by a cone with a half-cone angle equal in value to the angle at the sheet break up point. This assumption is made because the larger droplets, as mentioned previously, will maintain their path from the breakup point while the smaller droplets are dragged towards the center axis at $r = 0$. Therefore, this defines the theoretical maximum radial location at which droplets will be found. Obviously in practical situations there will be some small portion of droplets outside of this zone due to turbulence and other physical phenomena, but as experiment has shown, the number of droplets die off rapidly at further radial locations (Saha et al.). Additionally, the entire flow field is assumed axisymmetric about the center axis and all relevant variables being calculated are assumed constant across each cross-section. This effectively makes it so that all subsequent calculations need to be made only in the axial direction. While this assumption is not exactly true, it holds well for this problem since only the mean global diameter, defined by the SMD, is being calculated at each axial location.

All assumptions relevant to the equations at hand will be listed explicitly in their respective sections, but some overall problem approximations should be noted. In this problem, it will be assumed that there is no heat or mass transfer (non-condensing environment) between the droplets and gaseous medium. In addition, no turbulence will

be accounted for in any section of the problem. Finally, all gravitational effects and fictitious forces on the droplets will also be neglected. In the next section, the work of Lee and Robinson will be extended for pressure swirl atomizers to calculate the cross-sectional Sauter mean diameter.

III. Energy Conservation and Sauter Mean Diameter:

To begin, the continuity statement is applied from the injector orifice to a cross-section far enough downstream where all primary and secondary atomization processes are complete, and all the liquid is in spherical form.

$$\rho_L Q = \int_0^R \int_0^\infty n \rho_L \frac{\pi}{6} D^3 u_z \frac{d\overline{n}}{dD} 2\pi r dD dr \tag{6}$$

Q, Uz, dn/dD, and n in Eq. 6 represent the volumetric flow rate at the injector, the axial component of the droplet velocity, the droplet number distribution, and the drop number density at a downstream location, respectively. The volumetric flow rate will be defined later in this section. Taking the axial velocity to be constant at the cross-section and cancelling the liquid density, an equation for the droplet concentration can be derived.

$$n = \frac{Q}{\frac{\pi}{6} u_z \int_0^R \int_0^\infty D^3 \frac{d\overline{n}}{dD} 2\pi r dD dr} \tag{7}$$

Based on the assumptions given in the last section in regards to the control volume, the radius at each cross section is defined by Eq. 8.

$$R = z \tan \theta_b \tag{8}$$

Neglecting the heat transfer, potential energy, and the internal energy, the energy equation for the liquid phase in pressure-swirl atomizers is given by the following equation.

$$\Delta KE = \dot{W} + E_{\sigma} + \varepsilon \tag{9}$$

Where the term on the left represents the rate of change of the total kinetic energy, and the right-hand-side terms represent the work rate, surface tension energy, and viscous dissipation, respectively. The surface tension energy is an extra term that must be added due to the droplets that are formed downstream of the nozzle. The work term in Eq. 9 represents the work done by the air on the droplets as they traverse in the axial direction. Finally, the viscous dissipation represents the relative kinetic energy dissipated into heat. If constant cross-sectional velocities are assumed, the rate of change of kinetic energy can be represented by

$$\Delta KE = \frac{1}{2}\rho_L Q U_{K-inj}^2 - \int_0^R \int_0^{\infty} \frac{1}{2}\rho_L n \frac{\pi}{6} D^3 u_z U_K^2 \frac{d\bar{n}}{dD} 2\pi r dD dr \tag{10}$$

Here $U_{K\text{-inj}}$ and U_K represent the total liquid kinetic energy at the injector and at a downstream location, respectively. Substituting Eq. 7 for n and simplifying, the rate of change of the total kinetic energy is given as

$$\Delta KE = \frac{1}{2}\rho_L Q\left[U_{K-inj}^2 - U_K^2\right] \tag{11}$$

The surface tension energy term can be defined in a similar manner and is given in Eq. 12.

$$E_{\sigma} = \int_0^R \int_0^{\infty} n\sigma\pi D^2 u_z \frac{d\bar{n}}{dD} 2\pi r dD dr \tag{12}$$

Substituting for the droplet concentration term and simplifying as before will give the surface tension energy term as a function of the volumetric flow rate, the surface tension, and the Sauter mean diameter.

$$E_\sigma = 6\sigma Q \frac{\int_0^R \int_0^\infty D^2 \frac{d\bar{n}}{dD} 2\pi r dD dr}{\int_0^R \int_0^\infty D^3 \frac{d\bar{n}}{dD} 2\pi r dD dr} = Q\frac{6\sigma}{SMD} \tag{13}$$

As mentioned previously, the rate of work term arises due to the work done on the liquid droplets from the point of break up to the desired axial location by the aerodynamic drag. This term can be represented as a double integral and is given by the following:

$$\dot{W} = \int_{Z_0}^{z} \int_0^R \int_0^\infty n F_D U_R \frac{d\bar{n}}{dD} 2\pi r dD dr dz \tag{14}$$

Where F_D is the total drag force in the z, r, and θ directions and U_R is the total relative velocity between the droplet and the gas. Strictly speaking, the work done on the liquid during primary atomization should also be included; however, the viscous effects during primary atomization will not be accounted for in this paper due to reasons that will be described in the next section. In that case, Eq. 14 represents the total work done on all the droplets from Z_0 to z. The total drag force can be represented as the sum of the force in each direction as given by

$$F_D = F_{D_z} + F_{D_r} + F_{D_\theta} \tag{15}$$

The drag force in each direction is generally represented in the form of a drag coefficient and is given by

$$F_{D_Z} = -\frac{1}{2}\rho_g \frac{\pi}{4} D^2 U_R \left(u_z - \upsilon_z\right) C_D \tag{16}$$

$$F_{D_r} = -\frac{1}{2}\rho_g \frac{\pi}{4} D^2 U_R \left(u_r - \upsilon_r\right) C_D \tag{17}$$

$$F_{D_\theta} = -\frac{1}{2}\rho_g \frac{\pi}{4} D^2 U_R \left(u_\theta - \upsilon_\theta\right) C_D \tag{18}$$

Here the u terms represent the liquid velocity, whereas the v terms represent the gaseous velocity. Also, U_R must be used due to the way that the coefficient of drag is generally defined. The total relative velocity can be acquired through the following equation.

$$U_R = \sqrt{\left(u_z - \upsilon_z\right)^2 + \left(u_r - \upsilon_r\right)^2 + \left(u_\theta - \upsilon_\theta\right)^2} \tag{19}$$

Taking Eq. 7 and 15-19 and substituting them into Eq. 14 and simplifying, the following relation for the work term can be derived.

$$\dot{W} = -\frac{3}{4}\rho_g \int_{Z_0}^{z} \frac{Q}{SMD}\frac{U_R^2}{u_z} C_D \left[\left(u_z - \upsilon_z\right) + \left(u_r - \upsilon_r\right) + \left(u_\theta - \upsilon_\theta\right)\right] dz \tag{20}$$

The usual practice is to take the coefficient of drag from empirical formulas. There are a myriad of different equations that relate C_D with the droplet Reynolds number for different ranges of Re. Unfortunately, not all of them are easily numerically integrated (Lefebvre, *Atom. & Sprays*). This is due to the fact that there is no one empirical relation that is valid for the entire range of Reynolds numbers, therefore multiple equations have to be used. Using multiple equations will generally introduce *if, else* statements in the numeric solver which introduces numerical discontinuities and can drastically slow down the simulation. In this paper a more numerically tractable equation will be used that is fairly accurate for Re $\leq$ 1000 (Lefebvre, *Atom. & Sprays*). This is valid for most situations as the droplet Reynolds numbers don't, in general, reach such high values. For solutions that will be presented later, all Reynolds number values were checked to ensure

that none go above Re = 1000. The equation for the drag coefficient taken from Lefebvre is given as (*Atom. & Sprays*)

$$C_D = \frac{24}{\mathrm{Re}}\left[1+\tfrac{1}{6}\mathrm{Re}^{2/3}\right] \tag{21}$$

Where the droplet Reynolds number is defined as

$$\mathrm{Re} = \frac{U_R SMD}{\nu_g} \tag{22}$$

In this analysis, no account will be made for internal mechanisms of the droplet such as internal circulation or droplet deformation, therefore, the only form of viscous dissipation that can occur and be consistent with the present model is the kinetic energy that is dissipated in the small boundary layer near the droplet surface (see fig. 9.). This can be visualized in the following manner; in the boundary layer, a small portion of the relative kinetic energy between the droplet and the gas will be dissipated into heat. This heat will have the final result of increasing the droplet's temperature which effectively increases its internal energy. This can be seen more directly by inspecting the boundary layer energy equation (Schlichting and Gersten).

$$\rho c_p\left(u\frac{\partial T}{\partial x}+v\frac{\partial T}{\partial y}\right)=\frac{\partial}{\partial y}\left(\lambda\frac{\partial T}{\partial y}\right)+\beta T u\frac{dp}{dx}+\mu\left(\frac{\partial u}{\partial y}\right)^2 \tag{23}$$

Note that in Eq. 23, the notation used is not the same as that given previously. Here, if a plane coordinate is assumed, x and y represent the tangential and normal directions, respectively. In the same manner, u and v are the tangential and normal velocities. Here, T represents the temperature in the boundary layer, P the pressure, and ρ, μ, λ, β, and C_p are the gas density, gas viscosity, thermal conductivity, thermal expansion coefficient, and isobaric specific heat capacity, respectively. From Eq. 23, it is evident that even if

there is no heat transfer to the body, the viscous dissipation (given by the last term) will form a thermal boundary layer (Schlichting and Gersten 226) near the surface. For the most ideal case, even if the wall is adiabatic, the dissipation of kinetic energy would have the final result of increasing the temperature at the wall to a value above its surrounding (Schlichting and Gersten 226). This explanation is given in order to explain the physical mechanism behind the dissipation in the boundary layer of the droplet and justify the reasoning behind the dissipation model; however, the solution for the SMD is only concerned with the overall energy budget (such as how much energy was dissipated) of the liquid phase and not in the exact physical mechanism in which it increased or decreased the mean diameter. Observing Eq. 23, it is obvious that the viscous dissipation will be proportional to the gas-phase viscosity and not the liquid phase, and will be a function of the velocity profile in the boundary layer. It should also be noted that, if in the future mass transfer between the droplet and gas is to be accounted for, it will be critical that a corrected viscosity coefficient be used that accounts for the vapor phase.

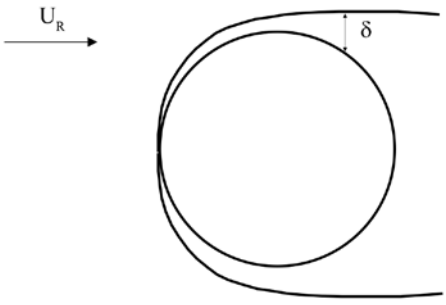

Fig. 9. Droplet Boundary Layer. Figure defines the boundary layer of a single droplet.

In the present analysis, instead of doing detailed calculations in order to determine the velocity profile in the boundary layer, an order of magnitude analysis will be done in its place. Before assessing the total dissipated energy, it is beneficial to first assess how the energy dissipates for a single droplet. For the simple unidirectional, plane boundary case, the dissipation of kinetic energy per unit volume is given as,

$$\frac{\varepsilon}{V} = \mu_g \left(\frac{\partial u}{\partial y} \right)^2 \tag{24}$$

Where V is the representative volume. Based on this equation, an order of magnitude analysis yields that the dissipation per unit volume should scale with respect to the velocity drop across the boundary layer and the boundary layer length. Making these approximation, Eq. 24 becomes

$$\frac{\varepsilon}{V} \approx \mu_g \frac{U_{scale}^2}{\delta^2} \tag{25}$$

Where δ is the boundary layer length. Due to the fact that all three velocity components are present for the droplet and that the actual boundary layer flow is significantly more complex over a droplet than flow over a flat wall, Eq. 25 will not be strictly applicable for the current problem. With that in mind, this equation should be fairly valid for a first-order analysis provided that a constant parameter is included. Taking the scale velocity to be the total relative velocity between the droplet and the gas, as defined by Eq. 19, the kinetic energy dissipated per droplet can be written as

$$\varepsilon_{drop} \approx K \mu_g \frac{U_R^2}{\delta^2} V \tag{26}$$

Where K is a constant parameter used in the model. Now the volume over which this energy is dissipated should be proportional to the portion of the surface area that is

affected by the boundary layer times the boundary layer length. This surface area will be taken as the total surface area of the droplet. This is obviously not exactly true for two reasons; 1) the boundary layer length is not constant across the droplet and 2) due to flow separation and other physical phenomena, the surface area which is affected by the boundary layer is not exactly the total surface area of the droplet. Nevertheless, this error should be on the same order as the other approximations taken in this problem. Including this volume, Eq. 26 becomes

$$\varepsilon_{drop} \approx K\mu_g \frac{U_R^2}{\delta^2}\pi D^2 \delta = K\mu_g \frac{U_R^2}{\delta}\pi D^2 \tag{27}$$

The boundary layer length over a spherical droplet has been shown (Rosenhead) to be on the order of

$$\delta = \sqrt{\frac{\nu_g SMD}{U_R}} \tag{28}$$

It is important to keep in mind that the current dissipation analysis is valid for droplet Reynolds numbers >> 1 (or strictly speaking, as Re goes to ∞), and that values of Re near or less than one will not adhere to the same derivation. Experimental observation has shown that these orders of magnitude should hold for Re > 10 (Rosenhead). Using Eq. 29 in Eq. 28, the viscous dissipation term per droplet can be derived as

$$\varepsilon_{drop} \approx K\mu_g \frac{U_R^2 U_R^{1/2}}{\sqrt{\nu_g SMD}}\pi SMD^2 \tag{29}$$

In order to get the total energy dissipated, this equation needs to be integrated over all droplets and over the entire control volume.

$$\varepsilon = \int_{Z_0}^{z}\int_{0}^{R}\int_{0}^{\infty} n\varepsilon_{drop}\frac{d\bar{n}}{dD} 2\pi r dD dr dz \tag{30}$$

Substituting the droplet dissipation and the droplet concentration into Eq. 31 and simplifying, the total viscous dissipation term can be derived.

$$\varepsilon = 6K\mu_g \int_{Z_0}^{z} \frac{Q}{SMD^2} \frac{U_R^2}{u_z} \mathrm{Re}_d^{1/2}\, dz \tag{31}$$

Where Re_d is the droplet Reynolds number and is defined by

$$\mathrm{Re}_d = \frac{U_R SMD}{\nu_g} \tag{32}$$

Taking all the energy terms and substituting them into Eq. 11, cancelling out Q, and simplifying, a relationship for the Sauter mean diameter can be formulated.

$$\begin{aligned} \frac{1}{2}\rho_L\left[U_{K-inj}^2 - U_K^2\right] &= \frac{6\sigma}{SMD} + 6K\mu_g \int_{Z_0}^{z} \frac{1}{SMD^2} \frac{U_R^2}{u_z} \mathrm{Re}_d^{1/2}\, dz - \ldots \\ &\frac{3}{4}\rho_g \int_{Z_0}^{z} \frac{1}{SMD} \frac{U_R^2}{u_z} C_D\left[\left(u_z - \upsilon_z\right) + \left(u_r - \upsilon_r\right) + \left(u_\theta - \upsilon_\theta\right)\right] dz \end{aligned} \tag{33}$$

This is an algebraic equation for the SMD that can be solved provided that the velocity history of the droplets are known. Before the exact methodology for Eq. 33 is discussed, it is important to derive the equations for the droplet and air velocities.

IV. Thin Sheet Analysis:

If the assumption is made that the sheet ejecting from the injector orifice is much thinner than the injector diameter, then it is reasonable to approximate that the liquid velocity is constant across the conical cross-section. It will also be assumed that all viscous interactions with the air are negligible. This is a reasonable assumption due to the liquid's high density which prevents it from slowing down too drastically during the primary atomization process. It should be noted that, if required, calculating the liquid

kinetic energy loss in this region is mathematically feasible provided that axisymmetric flow is assumed. It is readily seen that for the case with no swirl, Mangler coordinate transformation can be made to turn the analysis into the simple plane flow analysis (Rosenhead; Schlichting and Gersten; Goldstein). If the third velocity component is added, the problem becomes more complicated; despite this, it should be possible to apply Pohlhausen's integral approximation to calculate the boundary layer velocity profile and the skin friction coefficient. Pohlhausen's method has seen success when applied to the internal swirl chamber of pressure-swirl atomizers (Binnie and Harris).

For this problem, it is beneficial to take a more natural coordinate system as defined by fig. 10. Here, the coordinate s represents the path along the meridian, r the local radius from the central axis, and r_c the radius of curvature. In addition, t is taken to be the sheet thickness, θ the local angle tangent to the meridian, U the total velocity of the sheet, U_θ the swirl component of velocity, ΔP the pressure change across the sheet, and g the gravitational acceleration. Taking a small section of the sheet and performing a normal force balance across it yields the following relationship.

$$\frac{2\sigma}{r_c}+\frac{2\sigma\cos\theta}{r}-\Delta P+\rho_L g t\sin\theta-\frac{\rho_L t U^2}{r_c}-\frac{\rho_L t U_\theta^2\cos\theta}{r}=0 \qquad (34)$$

The first two terms are due to the effects of surface tension, the third term is the effect of the pressure drop, the fourth term is due to gravitational effects, and the last two terms are from the centrifugal accelerations of the velocities. For the current problem, the gravity and pressure drop across the sheet are neglected. The first assumption is reasonable provided that the velocity components are much greater than the effects of gravity. The second assumption, however, has been shown to be inaccurate for some cases due to the

fact that the liquid motion does induce a noticeable amount of velocity in the air cavity (Parlange). This would effectively alter the shape of the conical sheet by a small amount.

Since the viscosity of the air is neglected, the energy equation can be used to state the relationship between the velocity components.

$$U^2 + U_\theta^2 = U_{z0}^2 + U_{\theta 0}^2 \tag{35}$$

Where the 0 subscript denotes conditions at the injector orifice. Conservation of angular momentum can then be used to see how the swirl velocity develops as the sheet expands.

$$U_\theta = \frac{U_{\theta 0} r_0}{r} \tag{36}$$

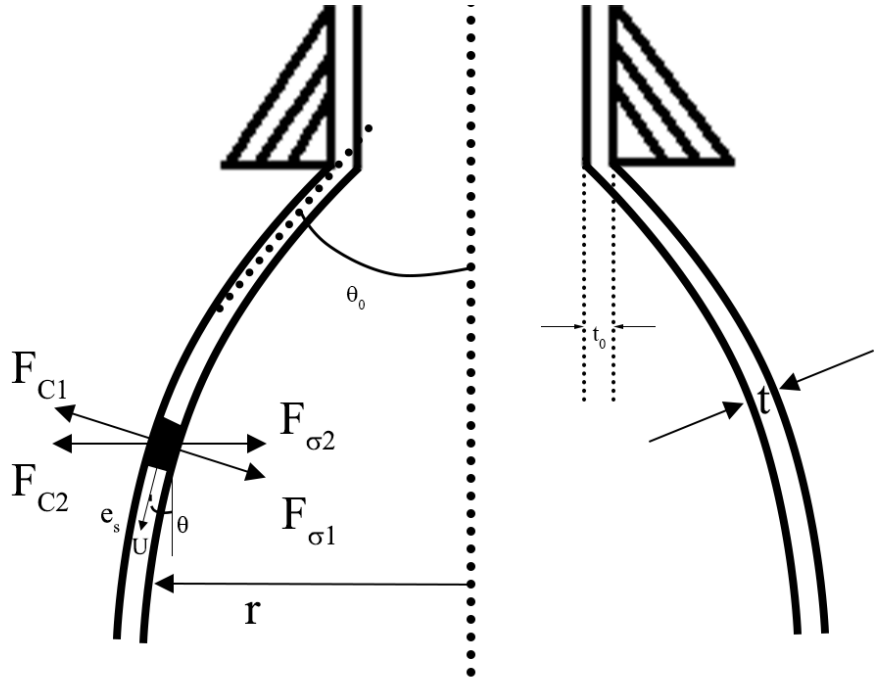

Fig. 10. Thin-Sheet Diagram. Figure defines the forces and necessary variables for the thin-sheet analysis.

In this paper, the axial and swirl component of velocity will be taken to equal

$$U_{z0} = U_{inj} \cos\theta_0 \tag{37}$$

$$U_{\theta 0} = U_{inj} \sin\theta_0 \tag{38}$$

Where U_{inj} is given by

$$U_{inj} = C_{dis}\sqrt{\frac{2\Delta P_{inj}}{\rho_L}} \tag{39}$$

C_{dis} represents the discharge coefficient and ΔP_{inj} is the injection pressure. For the validation section, if the injector velocity is measured and given, then that will be used instead of Eq. 39. Substituting Eq. 37 and 38 into Eq. 35 and 36, the following relationship for the local meridional and swirl velocity can be arrived at.

$$U = U_{inj}\sqrt{1-\sin\theta_0{}^2\,\frac{r_0^2}{r^2}} \tag{40}$$

$$U_\theta = \frac{U_{inj}\sin\theta_0 r_0}{r} \tag{41}$$

The statement of continuity across the sheet cross-section gives

$$Q = 2\pi r t U \tag{42}$$

This can then be solved for the sheet thickness to get

$$t = \frac{Q}{2\pi r U} \tag{43}$$

For the model validation section, if the experimental mass flow rate is not given, the sheet thickness can be calculated by the following:

$$t = t_0 \frac{U_{inj}}{U}\frac{r_0}{r} \tag{44}$$

Where the initial sheet thickness is computed from the following empirical relationship (Lefebvre, *Atom. & Sprays*):

$$t_0 = 3.66\left(\frac{\dot{m}D_{inj}\mu_L}{\Delta P_{inj}\rho_L}\right)^{1/4} \tag{45}$$

In general, Eq. 46 has to be iteratively calculated. From geometrical considerations, the following three relationships for the radius of curvature, the local radius, and the axial location can be derived.

$$\frac{1}{r_c} = -\frac{d\theta}{ds} \tag{46}$$

$$\frac{dr}{ds} = \sin\theta \tag{47}$$

$$\frac{dx}{ds} = \cos\theta \tag{48}$$

Finally, taking these relationships and substituting them back into Eq. 34, a system of ordinary differential equations can be acquired that describe the kinematics of the conical sheet.

$$\frac{d\theta}{ds} = \frac{\cos\theta}{r}\frac{\left[2\sigma - \rho_L t U_\theta^2\right]}{\left[2\sigma - \rho_L t U^2\right]} \tag{49}$$

$$\frac{dr}{ds} = \sin\theta \tag{50}$$

$$\frac{dx}{ds} = \cos\theta \tag{51}$$

These equations can then be solved from s = 0 to the point of sheet breakup. The initial conditions are given by the initial cone angle, the injector radius, and x = 0. The cone

angle, radius, and velocities at the point of break up can then be used as inputs for the droplet portion of the calculations. The axial and radial velocities are defined by

$$u_z = U\cos\theta \tag{52}$$

$$u_r = U\sin\theta \tag{53}$$

It should be noted once again that no instability mechanisms were accounted for, consequently, these equations represent the *average* properties of the conical sheet. Also, due to lack of time, no account was made to calculate the breakup point of the sheet, so the location has to be taken from experimental values. This is not too much of a setback, however, as the solutions calculated were not extremely sensitive to this value. In addition, the theory can be extended easily to include the breakup location calculation with sufficient mathematical derivation.

In the following section, the velocities of the droplet along with the air are derived in order to close the set of equations developed thus far.

V. Droplet Motion and Gas Entrainment:

In order to calculate the motion of the droplets, the droplets will be assumed to be in perfectly spherical form and that the droplet diameter remains constant from z = Z_0 to z. This effectively ignores the secondary atomization process. In addition, it will be assumed that the only force acting on the droplets is the aerodynamic drag. In this case, the force balance in all three directions can be written as

$$\int_0^\infty \rho_L \frac{\pi}{6} D^3 \frac{dn}{dD} dD \frac{du_z}{dt} = \int_0^\infty F_{D_z} \frac{dn}{dD} dD \tag{54}$$

$$\int_0^\infty \rho_L \frac{\pi}{6} D^3 \frac{dn}{dD} dD \frac{du_r}{dt} = \int_0^\infty F_{D_r} \frac{dn}{dD} dD \tag{55}$$

$$\int_0^\infty \rho_L \frac{\pi}{6} D^3 \frac{dn}{dD} dD \frac{du_\theta}{dt} = \int_0^\infty F_{D_\theta} \frac{dn}{dD} dD \tag{56}$$

Substituting Eq. 16-18 and noting that

$$\frac{du_i}{dt} = u_z \frac{du_i}{dz} \tag{57}$$

And simplifying, the equation of motion for the droplets in all three directions can be derived.

$$\frac{du_z}{dz} = -\frac{3}{4} \frac{\rho_g}{\rho_L} \frac{C_D}{SMD} \frac{U_R}{u_z} \left(u_z - \upsilon_z\right) \tag{58}$$

$$\frac{du_r}{dz} = -\frac{3}{4} \frac{\rho_g}{\rho_L} \frac{C_D}{SMD} \frac{U_R}{u_z} \left(u_r - \upsilon_r\right) \tag{59}$$

$$\frac{du_\theta}{dz} = -\frac{3}{4} \frac{\rho_g}{\rho_L} \frac{C_D}{SMD} \frac{U_R}{u_z} \left(u_\theta - \upsilon_\theta\right) \tag{60}$$

The drag coefficient is the same empirical relationship as defined before. It is given here again for convenience.

$$C_D = \frac{24}{\mathrm{Re}} \left[1 + \frac{1}{6} \mathrm{Re}^{2/3}\right] \tag{61}$$

$$\mathrm{Re} = \frac{U_R SMD}{\nu_g} \tag{62}$$

It is important to note here that the drag relation given above was empirically determined for *steady* flow over a sphere, but the droplets in this flow are constantly accelerating especially near the sheet breakup point where the relative velocity is the highest. Strictly speaking, the drag coefficient should be corrected to account for this,

though no such attempt is made in this paper. It is assumed that the droplet relaxation time is fast enough so that Eq. 61 holds. In order to calculate the air entrainment velocity in the axial direction, an integral method similar to the work by Cossali can be used. An integral momentum balance over the entire droplet control volume gives

$$\left[\int_0^R \rho_g \upsilon_z^2 2\pi r dr\right]_z - \left[\int_0^R \rho_g \upsilon_z^2 2\pi r dr\right]_{z=Z_0} = \int_{Z_0}^{z}\int_0^R\int_0^\infty n\left(-F_{D_z}\right)\frac{d\overline{n}}{dD}2\pi r dD dr dz \qquad (63)$$

Here the axial air velocity at Z_0 will be assumed to be approximately zero which cancels the second term in the above equation. This assumption is not exactly true due to the fact that the liquid motion of the sheet will induce an air velocity especially at the center core of the cone; nevertheless, in order to stay consistent with the previous portion of the model, the axial air velocity will be approximated as zero at the sheet breakup point. Substituting the axial drag term and the droplet concentration and simplifying gives the following relation

$$\upsilon_z^2 A = \int_{Z_0}^{z} \frac{3}{4} Q \frac{C_D}{SMD}\frac{U_R}{u_z}\left(u_z - \upsilon_z\right) dz \qquad (64)$$

By taking the derivative of both sides with respect to z and simplifying the equation, an ODE for the axial air velocity can be acquired.

$$\frac{d\upsilon_z}{dz} = \frac{3}{8}\frac{Q}{\upsilon_z A}\frac{C_D}{SMD}\frac{U_R}{u_z}\left(u_z - \upsilon_z\right) - \frac{\upsilon_z}{z} \qquad (65)$$

This equation has a discontinuity at $v_z = 0$, so for the numerical initial condition, the axial air velocity was set to be very close to zero, but not exactly at zero. Here Q can be taken to be of the same form as the one derived for the sheet portion of the model. It should also be noted that there should be some component of momentum added to Eq. 65 from

air entering from outside of the control volume, but this should be small in comparison to the motion induced by the droplets. The radial component of the gaseous velocity can be attained through a local mass balance relation (see fig. 11.). The mass balance gives

$$\int_{z_1}^{z_2} \rho_g \frac{V_e 2\pi R}{\cos\theta} dz = \int_0^R \rho_g \upsilon_{z2} 2\pi r dr - \int_0^R \rho_g \upsilon_{z1} 2\pi r dr \tag{66}$$

If the difference between z_1 and z_2 is taken to be small enough, the left hand side of the equation can be approximated as

$$\int_{z_1}^{z_2} \rho_g \frac{V_e 2\pi R}{\cos\theta} dz \approx \rho_g \frac{V_e 2\pi R_1}{\cos\theta} \Delta Z = \rho_g \upsilon_{z2} A_2 - \rho_g \upsilon_{z1} A_1 \tag{67}$$

Noting that

$$A = \pi R^2 \tag{68}$$

$$R = z \tan\theta \tag{69}$$

Eq. 67 can be simplified and solve for V_e to get

$$V_e = \frac{\sin\theta}{2 z_1 \Delta z} \left(\upsilon_{z2} z_2^2 - \upsilon_{z1} z_1^2 \right) \tag{70}$$

Then v_r can be computed from the following equation:

$$\upsilon_r = -V_e \cos\theta \tag{71}$$

As mentioned before, this relation holds only if ΔZ is sufficiently small. This was checked throughout all solutions by ensuring that the global continuity given by (assuming $v_z = 0$ at $z = Z_0$) Eq. 72 is satisfied.

$$\int_{Z_0}^{z} \rho_g \frac{V_e 2\pi R}{\cos\theta} dz = \rho_g \upsilon_z A \tag{72}$$

Essentially, the left hand side and the right hand side were computed at each axial location and checked that they are equal (see fig. 12.).

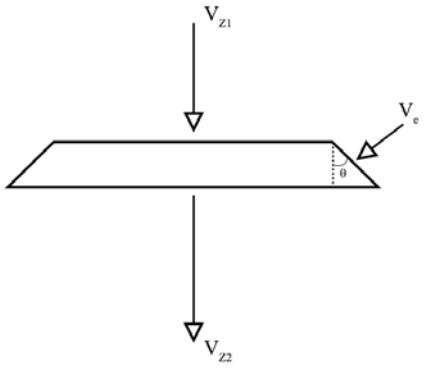

Fig. 11. Air Entrainment Control Volume.

In the figure, the 'exact' solution is given by the right-hand-side of Eq. 72. Both the linear and logarithmic plots are given to show how well the solution converges. From the plot, it is obvious that for the largest step size, both plots show a significant difference between the two calculations. As the step size is reduced, the two solutions converge at all points except near Z_0. This is due to the fact that there is a discontinuity in the calculations at Z_0, where V_e goes from zero to some value instantaneously. However, as the step size is reduced even further, the solutions on both the linear and logarithmic plots converge to the same line. This check method was *not* done manually when running large simulations. The algorithm will automatically check for this convergence and update the step size as needed.

For the tangential air motion, many different formulations were attempted, but no physically sound expression was reached. Due to this, the induced air motion in the tangential direction was simply assumed to be zero. While this is not exactly accurate, it does not affect the solutions drastically. This is because as the sheet expands, due to the conservation of angular momentum, the tangential component of velocity will have reduced significantly before the breakup point, and as a result, the induced air motion in the tangential direction should be much smaller than the other components.

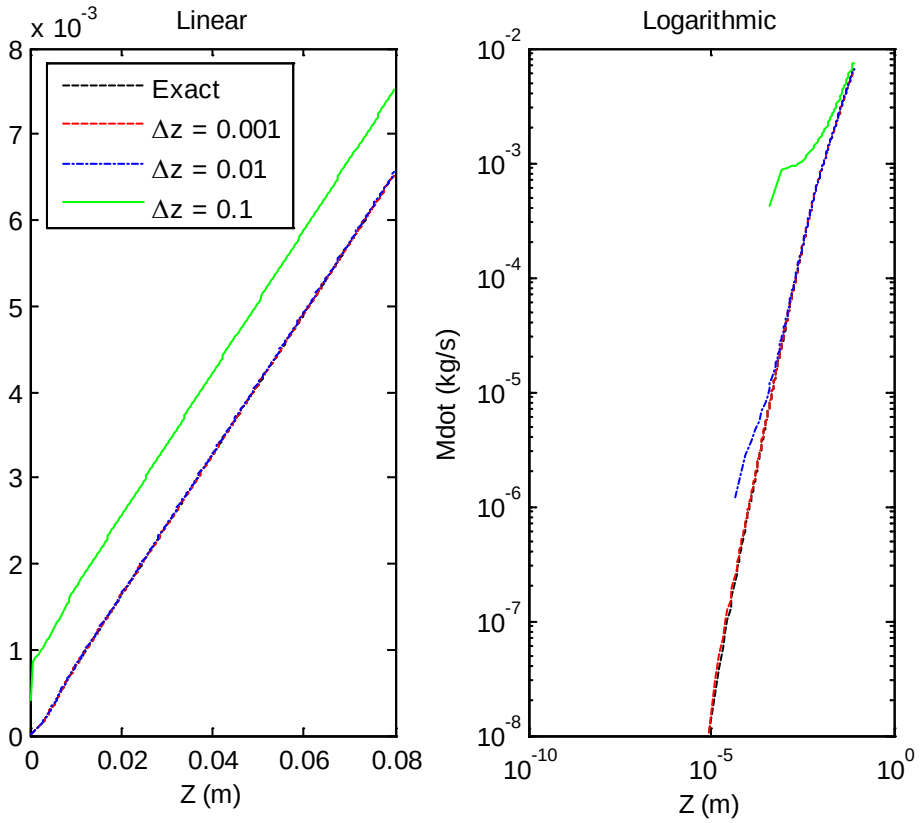

Fig. 12. Entrained Velocity Convergence. Plot depicting the convergence of the calculation for the entrained gas velocity.

Now that all the relationships for all the variables have been derived, they can be analyzed in detail. The full list of equations are listed below for convenience.

$$\frac{1}{2}\rho_L\left[U_{K-inj}^2 - U_K^2\right] = \frac{6\sigma}{SMD} + 6K\mu_g\int_{Z_0}^{z}\frac{1}{SMD^2}\frac{U_R^2}{u_z}\mathrm{Re}_d^{1/2}\,dz - \ldots$$
$$\frac{3}{4}\rho_g\int_{Z_0}^{z}\frac{1}{SMD}\frac{U_R^2}{u_z}C_D\left[\left(u_z-\upsilon_z\right)+\left(u_r-\upsilon_r\right)+\left(u_\theta\right)\right]dz \tag{73}$$

$$\frac{du_z}{dz} = -\frac{3}{4}\frac{\rho_g}{\rho_L}\frac{C_D}{SMD}\frac{U_R}{u_z}\left(u_z-\upsilon_z\right) \tag{74}$$

$$\frac{du_r}{dz} = -\frac{3}{4}\frac{\rho_g}{\rho_L}\frac{C_D}{SMD}\frac{U_R}{u_z}\left(u_r-\upsilon_r\right) \tag{75}$$

$$\frac{du_\theta}{dz} = -\frac{3}{4}\frac{\rho_g}{\rho_L}\frac{C_D}{SMD}\frac{U_R}{u_z}u_\theta \tag{76}$$

$$\frac{d\upsilon_z}{dz} = \frac{3}{8}\frac{Q}{\upsilon_z A}\frac{C_D}{SMD}\frac{U_R}{u_z}\left(u_z-\upsilon_z\right) - \frac{\upsilon_z}{z} \tag{77}$$

$$\upsilon_r = -\frac{\cos\theta\sin\theta}{2z_1\Delta z}\left(\upsilon_{z2}z_2^2 - \upsilon_{z1}z_1^2\right) \tag{78}$$

The initial conditions for this system of equations is given through the calculations from the equations for the thin-sheet analysis. This is an index-3 differential-algebraic system of equations. Obviously, there is no general analytical solution to this problem. Also, due to the discontinuities involved in the equations, normal differential-algebraic numerical methods cannot be employed. Consequently, an iterative method is chosen to solve the problem. While a full detailed solver methodology will be covered in a later section, it is important for the current discussion to note that an initial guess for the SMD will be made and the remaining calculations will be performed assuming that the guessed

value for the SMD remains constant from Z_0 to z. Once the velocities are calculated, a new SMD will be determined and the guess updated.

It is critical that the correct scales for this problem be determined and the problem restated in non-dimensional form, so that the proper relationship between the different parameters can be observed.

VI. Scaling:

As stated previously, for the plain-orifice injector, the SMD scales with the injector diameter. For the pressure-swirl atomizer, numerous experiments have shown that the initial sheet thickness heavily influences the SMD values (Lefebvre, “Pred. Saut. Mean Diam.”). Based on this consideration, it is evident that the correct length scale to normalize the SMD should be the initial sheet thickness. Second, since the atomizer’s purpose is to utilize the liquid kinetic energy to break up the bulk mass, then it is reasonable to take the total velocity at the injector to be the correct velocity scale for the problem. Finally, the gas density should also be an important factor, both in the primary atomization and secondary atomization, as it aids in the instability and disintegration of the liquid to droplets of decreasing size. Based on these arguments, the following scales will be chosen:

$$SMD^* = \frac{SMD}{t_0} \quad t^* = \frac{t}{D_{inj}}$$
$$\xi = \frac{z}{D_{inj}} \qquad \rho^* = \frac{\rho_g}{\rho_L}$$
$$U_i^* = \frac{U_i}{U_{inj}} \qquad r^* = \frac{r}{D_{inj}} \tag{79}$$
$$s^* = \frac{s}{D_{inj}}$$

Applying these scales and noting that the SMD is assumed constant for each iteration of the solution, the following non-dimensional equations can be derived.

SMD:

$$SMD^{*2} - \left[\frac{12\rho^*}{We\left(1-U_K^{*2}\right)} - \frac{3}{2}\frac{\rho^*}{t_0^*\left(1-U_K^{*2}\right)} \int_{\xi_0}^{\xi} \frac{U_R^{*2}}{u_z^*} C_D \left(\left(u_z^* - \upsilon_z^*\right) + \left(u_r^* - \upsilon_r^*\right) + u_\theta^* \right) d\xi \right] SMD^* \ldots$$
$$- \frac{12K}{\mathrm{Re}\, t_0^*\left(1-U_K^{*2}\right)} \int_{\xi_0}^{\xi} \frac{U_R^{*2}}{u_z^*} \mathrm{Re}_d^{1/2}\, d\xi = 0 \tag{80}$$

Entrainment:

$$\frac{du_z^*}{d\xi} = -\frac{3}{4}\frac{\rho^*}{t_0^* SMD^*} C_D \frac{U_R^*}{u_z^*}\left(u_z^* - \upsilon_z^*\right) \tag{81}$$

$$\frac{du_r^*}{d\xi} = -\frac{3}{4}\frac{\rho^*}{t_0^* SMD^*} C_D \frac{U_R^*}{u_z^*}\left(u_r^* - \upsilon_r^*\right) \tag{82}$$

$$\frac{du_\theta^*}{d\xi} = -\frac{3}{4}\frac{\rho^*}{t_0^* SMD^*} C_D \frac{U_R^*}{u_z^*} u_\theta^* \tag{83}$$

$$\frac{d\upsilon_z^*}{d\xi} = \frac{3}{8}\frac{1}{A^*\upsilon_z^*}\frac{C_D}{SMD^*}\frac{U_R^*}{u_z^*}\left(u_z^* - \upsilon_z^*\right) - \frac{\upsilon_z^*}{\xi} \tag{84}$$

$$\upsilon_r^* = -\frac{\cos\theta\sin\theta}{2\xi_1\Delta\xi}\left(\upsilon_{z2}^*\xi_2^2 - \upsilon_{z1}^*\xi_1^2\right) \tag{85}$$

Thin-Sheet Equations:

$$\frac{d\theta}{ds^*} = \frac{\cos\theta}{r^*}\frac{\left[2\rho^*/We - U_\theta^{*2}/2U^*r^*\right]}{\left[2\rho^*/We - U^*/2r^*\right]} \tag{86}$$

$$\frac{dr^*}{ds^*} = \sin\theta \tag{87}$$

$$\frac{d\xi}{ds^*} = \cos\theta \tag{88}$$

In the above equations We and Re are the Weber and Reynolds numbers and they are defined as

$$We = \frac{\rho_g U_{inj}^2 t_0}{\sigma} \tag{89}$$

$$\mathrm{Re} = \frac{\rho_L U_{inj} t_0}{\mu_g} \tag{90}$$

It is interesting to note that the liquid viscosity does not appear anywhere in the above equations. This is due to the fact that no account has been made for the internal behavior of the liquid phase such as internal circulation, secondary atomization, or instabilities. If these effects are included in future extension of this model, then the Reynolds number should be defined appropriately.

VII. Solver Methodology:

As stated before, due to the discontinuities present, this system of equations needs to be solved iteratively. The general procedure will be to first calculate the sheet portion of the spray up to the point of break. This distance will be taken from experiment. Once this is completed, it is then possible to acquire the initial conditions for the droplet portion of the spray from

$$u^*_{z-b} = U^*_b \cos\theta_b \tag{91}$$

$$u^*_{r-b} = U^*_b \sin\theta_b \tag{92}$$

$$u^*_{\theta-b} = \frac{\sin\theta_0}{2r^*_b} \tag{93}$$

Where the subscript b represents the value at the breakup point. Once these initial conditions are attained, an initial guess for the SMD value will be made and the droplet velocity history will be calculated up to the given axial distance. From this history, the work and dissipation terms are computed, and a new guess for the SMD is attained (see fig. 13.). This step is repeated until the error is below 10^{-6}. Extensive measures were taken to accelerate the iterative algorithm. In general, convergence was reached within 5-7 minutes. In the following chapter, the present model will be extensively validated through independent experiments. In addition, detailed assessment on the solution will be made in order to demonstrate the model's strengths and shortcomings.

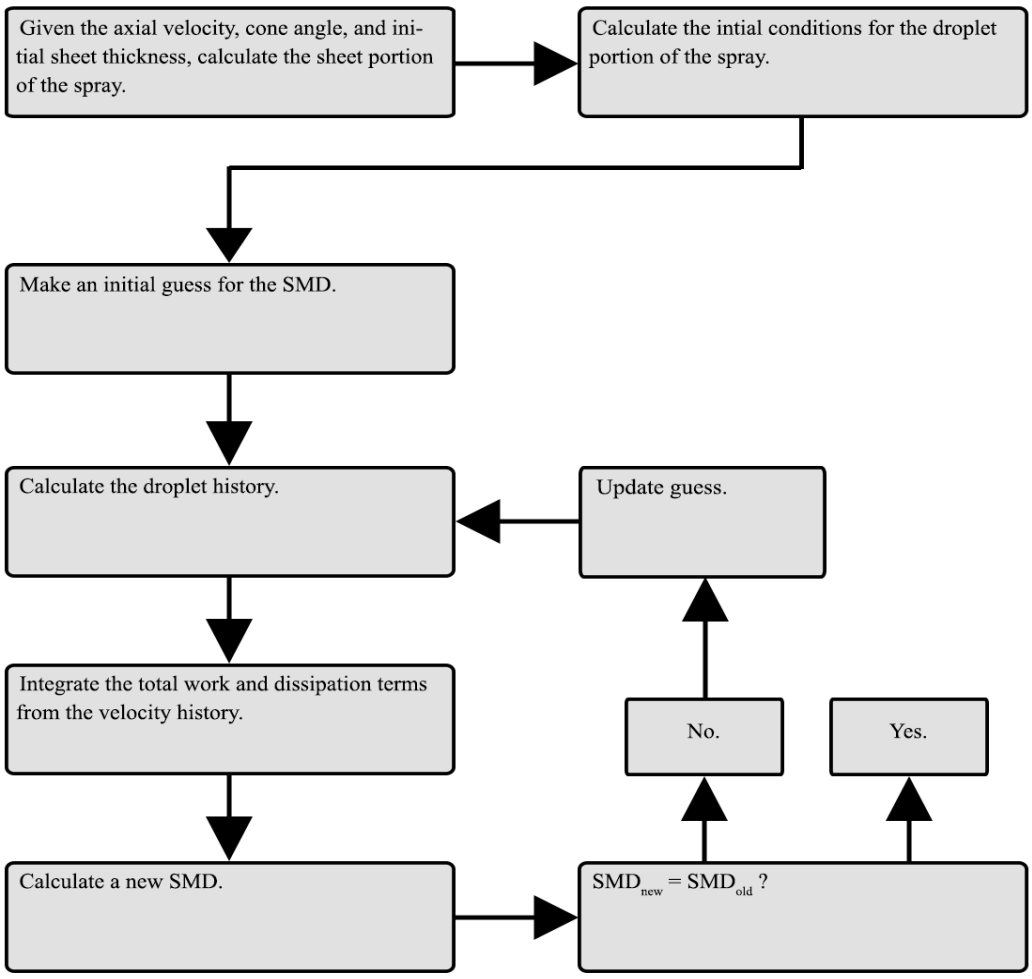

Fig 13. Solver Methodology. Figure depicts the logic behind numerical solver.

CHAPTER 3

VALIDATION OF MODEL

I. Overall Validation and Determination of Constant:

Tratnig and Brenn utilized phase-Doppler anemometry and photographic techniques to conduct 30 different experiments with pressure-swirl atomizers (Tratnig and Brenn). These experiments included varying atomizer internal geometry, liquid properties, and injection pressures. In order to provide sufficient initial conditions, the liquid properties, mass flow rate, and initial cone angle were measured directly. For the experiment, they measured the cross-sectional Sauter mean diameter as defined by

$$D_{32} = \frac{\sum_{j=1}^{J}\sum_{i=1}^{I} D_i^3\left(r_j\right)\dot{n}\left(r_j, D_i\right)2\pi r_j \Delta r}{\sum_{j=1}^{J}\sum_{i=1}^{I} D_i^2\left(r_j\right)\dot{n}\left(r_j, D_i\right)2\pi r_j \Delta r} \tag{94}$$

This is the exact definition used for the present model, so the comparison of the experimental results and the determination of the experimental constant, K, will be valid. In the above equation, D_i, r_j, and $\dot{n}$ are the droplet diameters, the radial location of the droplet, and the number flux of the droplet, respectively. The axial location at which the SMD values were measured was chosen so that all secondary atomization and coalescence effects were not present in the measurement. This is another reason this particular experiment is good for determining the experimental constant, as the current model does not account for either of those effects. The axial location chosen by Tratnig and Brenn is z = 80 mm for all trials. All trials were run for the same ambient air conditions given by ρ_g = 1.204 kg/m^3 and μ_g = 1.983*10^{-5} kg-s/m. Since the mass flow rate was given, the initial sheet thickness was calculated as

$$t_0^* = \frac{\dot{m}}{\rho_L \pi D_{inj} U_{inj}} \tag{95}$$

Where the injection velocity is calculated from

$$U_{inj} = C_{dis} \sqrt{\frac{2\Delta P}{\rho_L}} \tag{96}$$

The discharge coefficient was taken to be 0.5 which was acquired from the experiment. The sheet breakup length was experimentally measured with respect to the meridian. All the experimental and initial conditions used for the model validation are given in table 1 in the appendix. The relevant parameters, as defined by the current model, are given in non-dimensional form with the exception of the injector diameter and liquid viscosity.

The solution was computed for all 30 trials with a constant of K = 3.5. The dimensional SMD from the model and the experiment are plotted on linear and logarithmic scales in fig. 14 and 15, respectively. From the plots it is evident that the model can predict the correct values for the SMD fairly well for most of the experimental trials. It is clear from the plots that the model seems to do poorly for very low injection velocities. Upon closer inspection of the data, these same points correspond to extremely low Weber numbers and the lowest Reynolds numbers (see table 1 in appendix: Trail #3, 4, 7, and 8.). In addition to these points, the plots reveal that the slope of the model and the experiment coincide well except for two points at U_{inj} = 50.06 and 55.73 m/s. Assessing the dataset more closely indicates that these two points are for the two smallest cone angles.

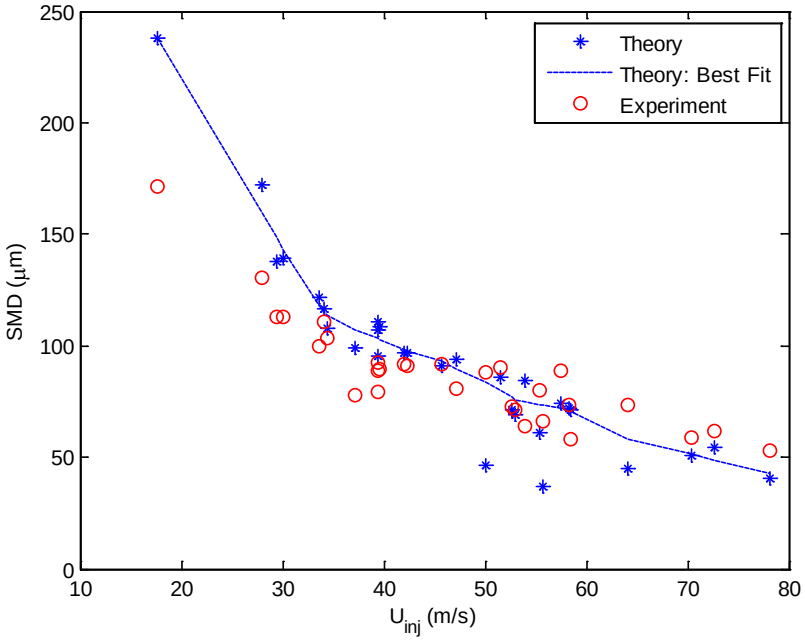

Fig. 14. Linear SMD Validation. A linear plot validating the SMD calculation of the model using experimental results by Tratnig and Brenn.

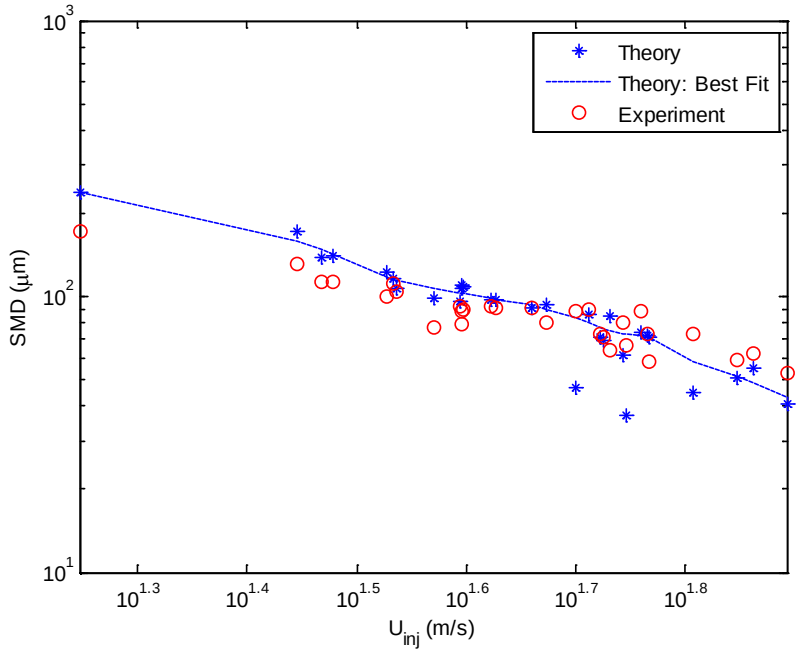

Fig. 15. Logarithmic SMD validation. A logarithmic plot validating the SMD calculation of the model using experimental results by Tratnig and Brenn.

It seems that the model does well for all cases except for extremely low values of injection velocity, or We and Re numbers, and smallest cone angles. It is of value to inspect what the sheet dynamical behavior is for the cases with the smallest angles. The radial and instantaneous cone angle plots for the two lowest initial cone angles of $\theta_0 = 7.5$ and $\theta_0 = 11.5$ are given below (see fig. 16 and 17.). It is clear from the plots that the sheet angle increases briefly before reaching a very small steady state value. This occurs due to the fact that for small initial cone angles, the swirl component of velocity is much smaller than the axial component, therefore there is less centrifugal acceleration to increase the cone angle. One of the reasons that the final SMD calculated by the model is inaccurate for these very low angles is that it was assumed that the entrainment area is defined by a cone with an angle equal to that at the sheet breakup point, but it has been shown (Ghosh and Hunt) that this is not true for very small cone angles. The entrainment area can be noticeably different in these cases and this behavior needs to be properly accounted for in the model. Finally, it is important to note that the non-dimensional initial sheet thickness, t_0^*, is very large for these two cases (on the order of 30-40% of the injector diameter). It is highly likely that these values are far too big to make the thin-sheet assumption, therefore introducing a certain level of error in the solution.

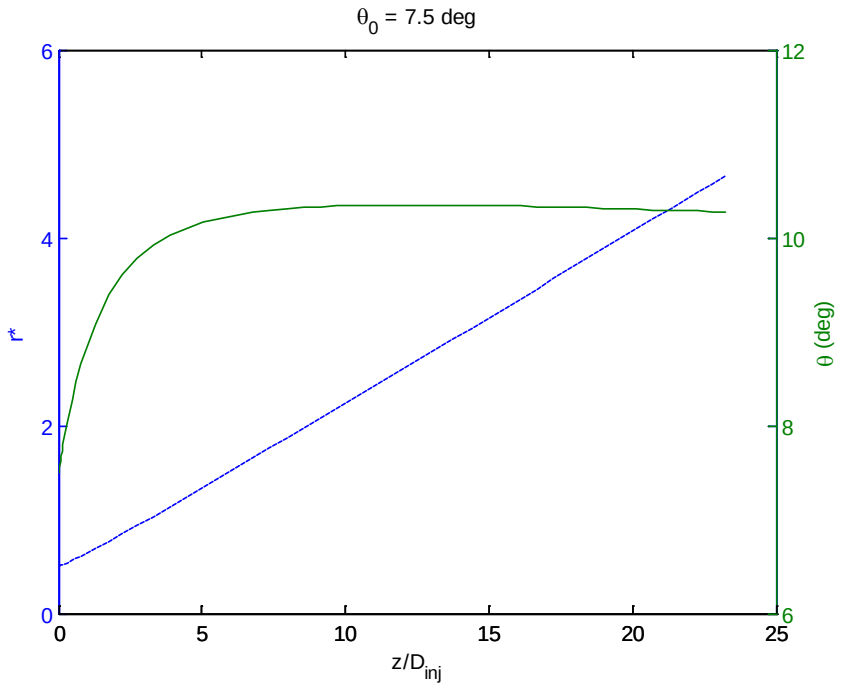

Fig. 16. Cone Angle Variation for Small Initial Angle. A plot of the instantaneous cone angle and dimensionless radius for θ_0 = 7.5 degrees.

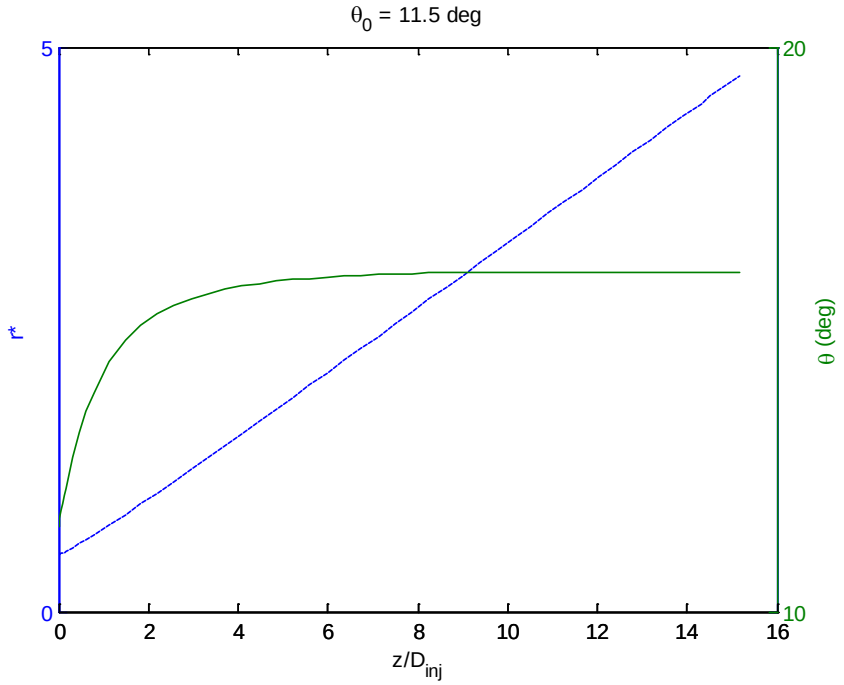

Fig. 17. Cone Angle Variation for Small Initial Angle. A plot of the instantaneous cone angle and dimensionless radius for θ_0 = 11.5 degrees.

II. Gas Entrainment:

Now that the calculations for the SMD has been validated, it is valuable to validate other aspects of the model to show the complete behavior of the solutions. Prosperi *et al.* conducted a particle-image velocimetry experiment using fluorescent tracers to measure the entrained gas velocity and mass flux. In their experiment, they used a *non-swirl* hollow-cone injector. However, since no account has been made for the tangential entrained velocity in the current model, the comparison between the sets of data will be valid if the tangential velocity is set to zero. The liquid used in the test is Isane IP 155, which is a non-evoporating iso-paraffin with properties similar to gasoline. They also varied the chamber gas density from 1.2 to 18 kg/m^3 in order to measure the effect of gas density on air entrainment. The mass flow rate given in their measurements is the same as defined by Eq. 72, which is repeated below for convenience.

$$\int_{z_0}^{z} \rho_g \frac{V_e 2\pi R}{\cos\theta} dz = \rho_g \upsilon_z A \tag{97}$$

The initial sheet thickness and cone angle were prescribed in the paper, so those values were used for the computation. The sheet breakup length was not explicitly states, so a small value of 1 mm was chosen. No account was made for the thin-sheet dynamics for these calculations, and the droplet computation was initiated from z = 1 mm with the conditions given at the injector orifice. The problem was solved by determining the SMD at the final axial location and integrating the velocity history for the mass flow at each axial location based on Eq. 97. The initial conditions for each trial including the converged solution for the SMD is given below (see table 2.). A discharge coefficient of 0.7 was used.

Table 1

Prosperi *et al.* initial conditions

Trial	D_{inj} (mm)	We	Re	$1/\rho^*$	t_0^*	Θ_0 (deg)	SMD^*
1	4.2	21.778	2.6369e+05	622.50	0.0238	40	1.0794
2	4.2	65.333	2.6369e+05	207.50	0.0238	40	0.6090
3	4.2	130.667	2.6369e+05	103.75	0.0238	40	0.4578

The solution for the three trials is presented in fig. 18. It is evident that the entrained mass-flow-rate calculations performed by the model are reasonably accurate. It should be noted that the experimental values had to be read from plots and so some human error may be present, though extensive measures were taken to minimize such errors through the use of pixel measurements in Adobe Photoshop. Finally, it is interesting to point out that the SMD values decrease rapidly with increase in ambient gaseous conditions, as expected. These calculations were all performed using the same constant as before (K = 3.5).

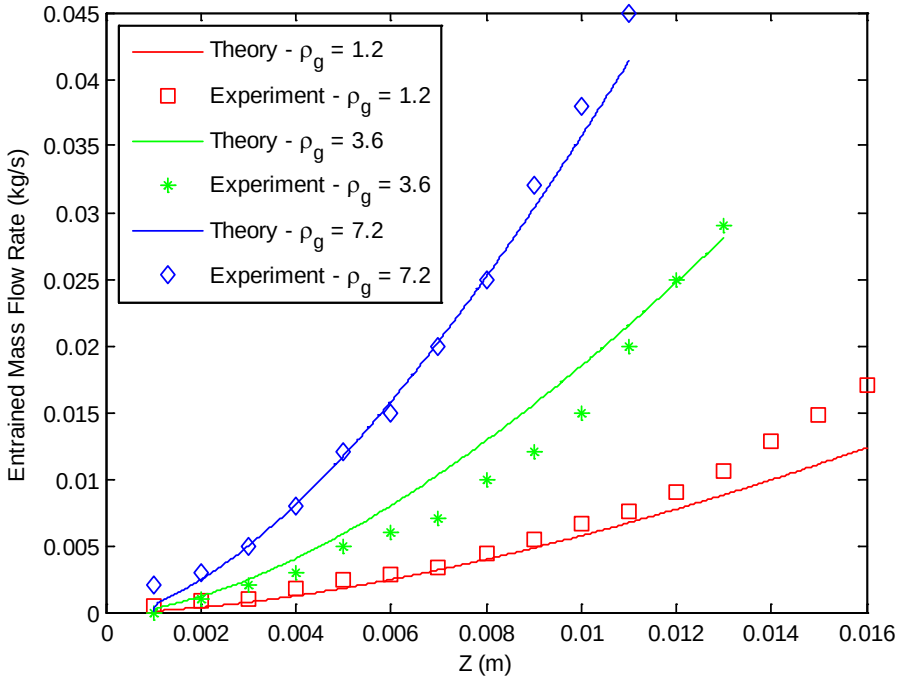

Fig. 18. Entrained Mass Flow Rate Validation. Plot of the entrained mass flow rate at various axial locations.

III. Droplet Velocity:

In order to get a complete picture of the model, it is important to also inspect the accuracy of the liquid velocity distribution across the spray. Unfortunately, this author had difficulty acquiring experiments that provided sufficient initial conditions to make a valid comparison of the model. The closest experiment found was the work of Saha *et al.* where they studied the breakup and coalescence of two different pressure-swirl atomizers. They used PDA and photographic techniques to measure the axial velocity, droplet diameter, and the initial cone angle. The test liquid and gas were water and air at standard conditions, respectively. While the experiment is compatible with the model, they only provided the arithmetic mean of the droplet diameters at the center axis and a few radial locations. In general, the cross-sectional SMD can be noticeable larger than the

arithmetic mean. This is especially true at the center axis as the air will drag the smaller droplets towards the center while the larger droplets will remain at the outer periphery. In the same regard, the velocity distribution across the cross section can vary appreciably from the center to the outer radius. Due to these reasons the comparison is not completely appropriate, but seeing that this was the only experiment found with somewhat relevant information, a comparison will still be attempted. Saha *et al.* performed experiments for two injector diameters, but they only provided sufficient information for only one of them, consequently the other will be disregarded in this comparison. The initial conditions used for this experiment are given below (see table 2.). Please note that the sheet breakup length is given with the respect to the axial direction and not the meridian.

Table 2

Saha *et al.* initial conditions

Trial	D_{inj} (mm)	We	Re	$1/\rho^*$	t_0^*	ξ_0^*	Θ_0 (deg)
1	0.3	2.2958	1.9881e+05	828.904	0.3747	6.333	35
2	0.3	4.0223	2.4880e+05	828.904	0.3350	6.333	37
3	0.3	5.7421	2.8688e+05	828.904	0.3119	6.333	39

The mass flow rate in these experiments was not provided. Accordingly, the initial sheet thickness had to be calculated from the empirical relationship given in the previous chapter. It should also be noted that the Weber numbers for these trials are in the same range where the model showed weakness in the Tratnig and Brenn validation by over predicting the SMD values. Taking into account the fact that the SMD is appreciably larger than the arithmetic mean, the droplet diameters at the center axis are usually

smaller than the outer periphery, and the fact that the model tends to over predict for very low Weber numbers, it is expected that the solution by the model should be noticeably larger than the data given by Saha *et al.* This was indeed the case when the model was ran for the constant K = 3.5. With this in mind, comparable results were able to be obtained by slightly reducing the constant parameter from K = 3.5 to K = 3.3 (see fig. 19-24.). While this is not exactly the proper way of making the comparison for the droplet diameter, it allows one to observe another important aspect of the model.

In the derivation of the model it was assumed that for the axial location being calculated, all droplets were in spherical form, or in other words, the primary and secondary atomization processes were complete. In addition, the model does not account for any droplet collisions or coalescence. Based on this, the model should become increasingly accurate as one traverses downstream from the nozzle up to the point of the completion of the atomization process. After which, the predicted SMD values should remain constant. Though, in reality, the droplets will have increased in size due to coalescence. Viewing fig. 19-21, one can see that this is exactly the case. For all Weber numbers, close to the sheet breakup location, the model significantly over predicts the droplet diameters, however, further out the model and experimental results converge to the same point. What is fascinating is that the model reaches a constant value for the droplet diameter at almost exactly the same location where the droplet coalescence begins. It should be noted that very near to the sheet breakup point, the model could not converge to a value and would blow up. As discussed in detail previously, this is simply due to the discontinuity at that point. Observing fig. 21, it is apparent that the experimental results for this Weber number behave very different than the others near the

nozzle. This is due to the fact that there is a high circulation zone near the nozzle which increases the probability of coalescence and subsequently increases the droplet diameters (Saha et al). The axial velocity results, fig. 22-24, show reasonable comparison as well, though it should be reiterated that the velocities at the center axis will be different than the ones at the outer periphery. The present model gives the solution for an average cross-sectional velocity based on an average diameter. Therefore, knowing the data at all radial locations would enable one to determine these values and make a much more valid comparison.

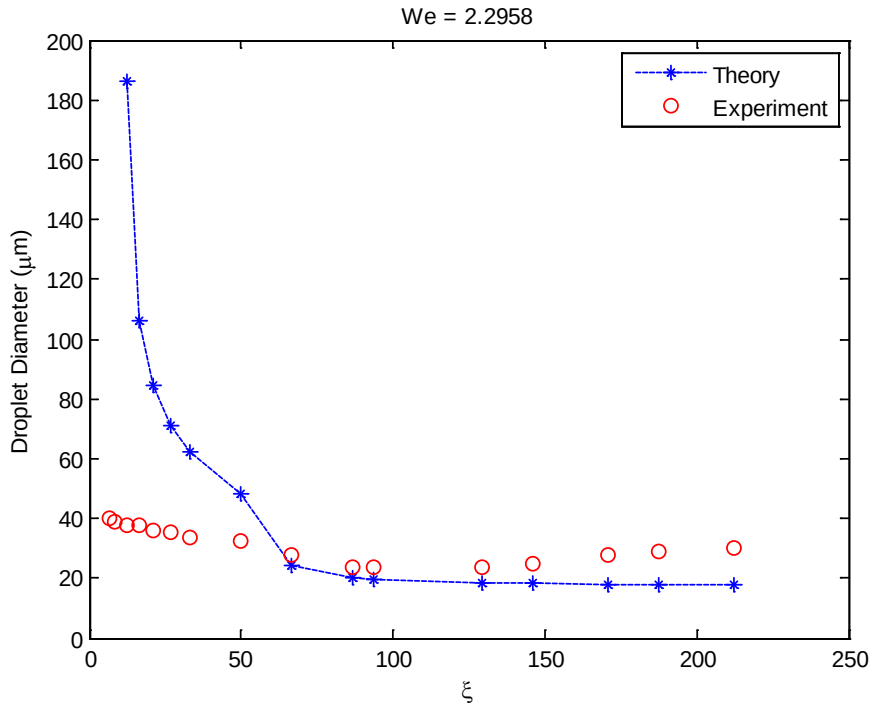

Fig. 19. Axial Variation of SMD. Plot of the SMD at various axial location for We = 2.2958.

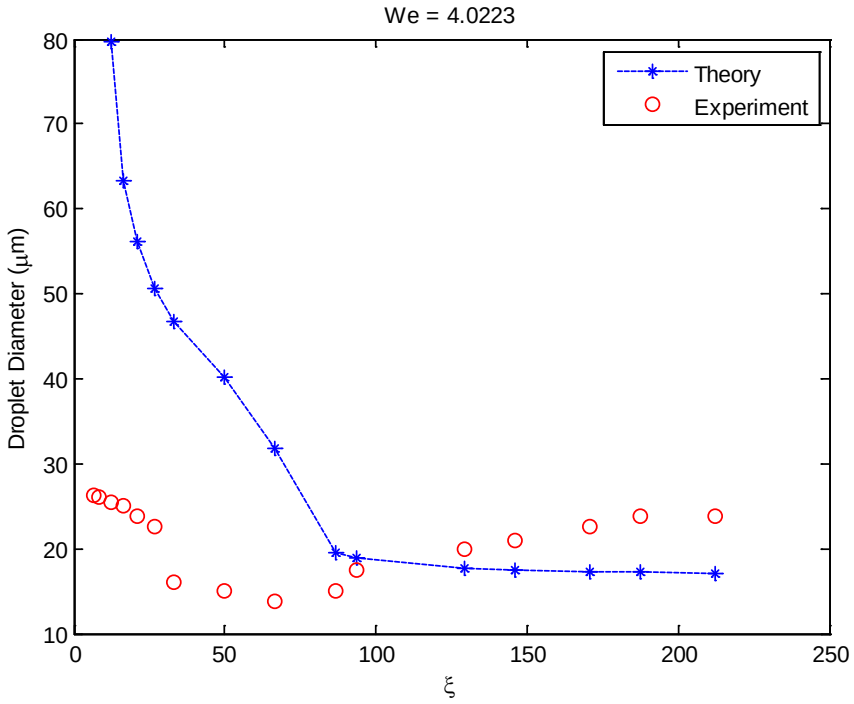

Fig. 20. Axial Variation of SMD. Plot of the SMD at various axial location for We = 4.0223.

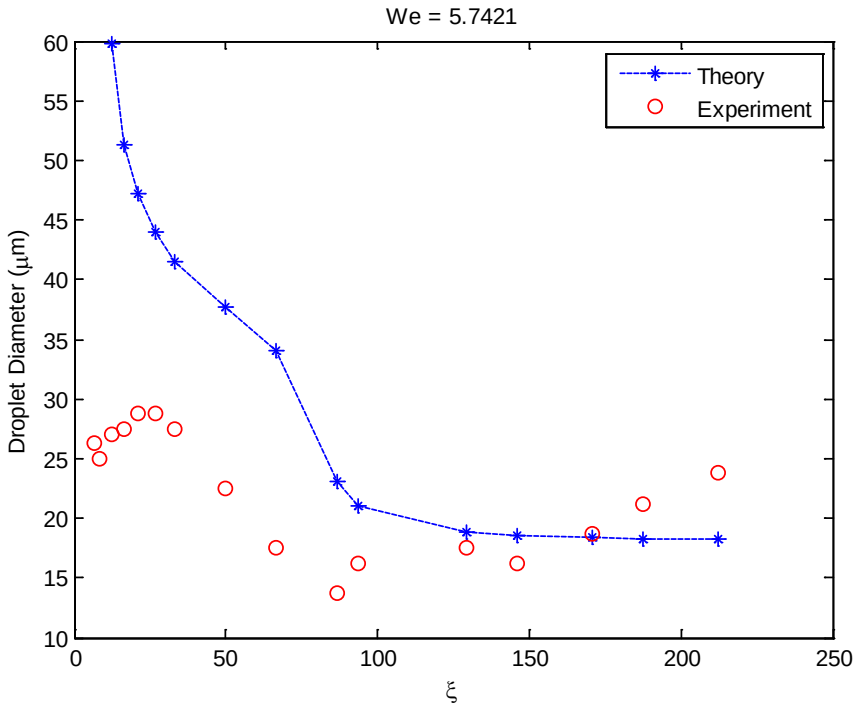

Fig. 21. Axial Variation of SMD. Plot of the SMD at various axial location for We = 5.7421.

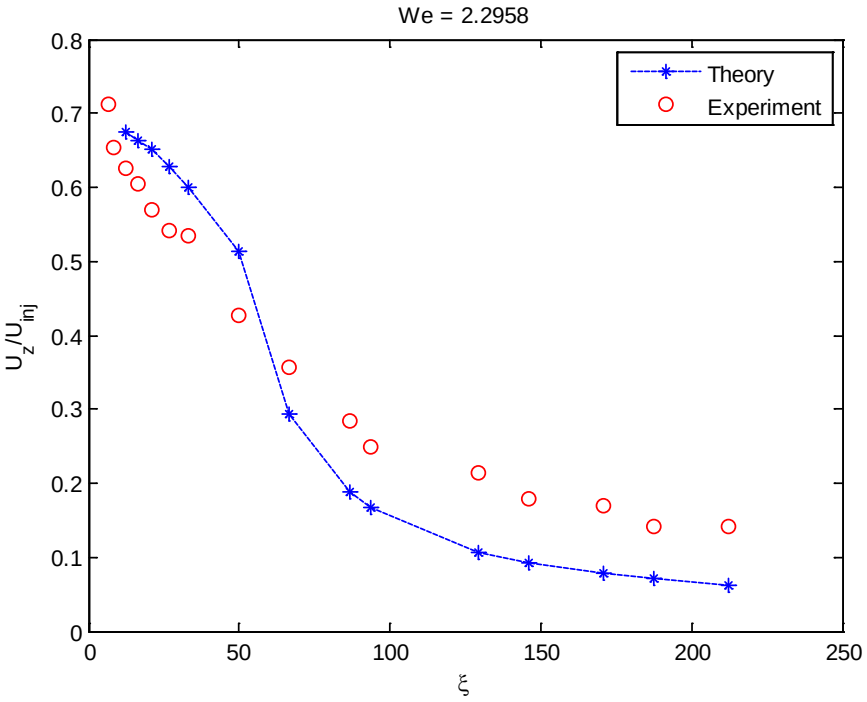

Fig. 22. Axial Variation of Axial Droplet Velocity. Plot of the droplet axial velocity at various axial location for We = 2.2958.

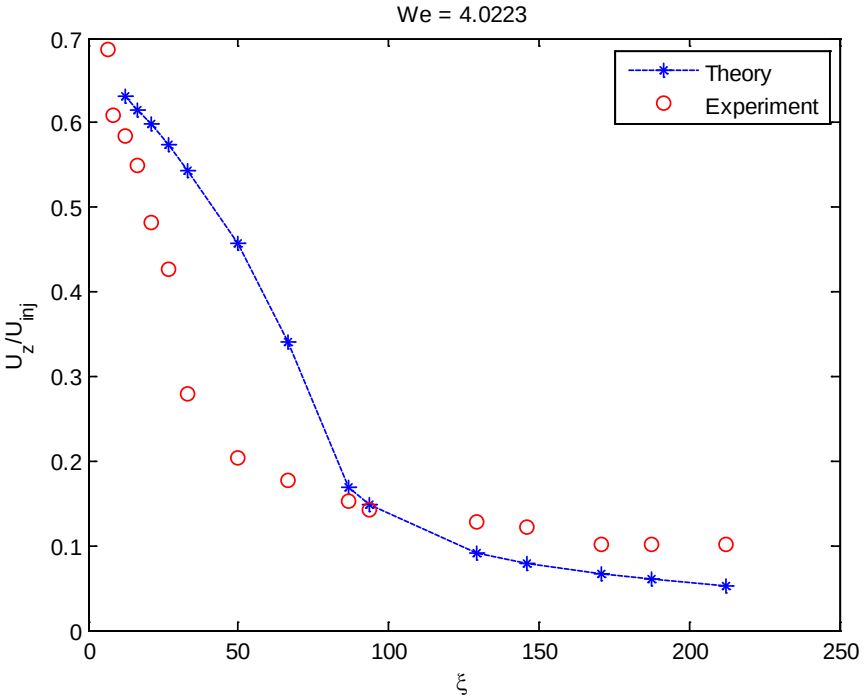

Fig. 23. Axial Variation of Axial Droplet Velocity. Plot of the droplet axial velocity at various axial location for We = 4.0223.

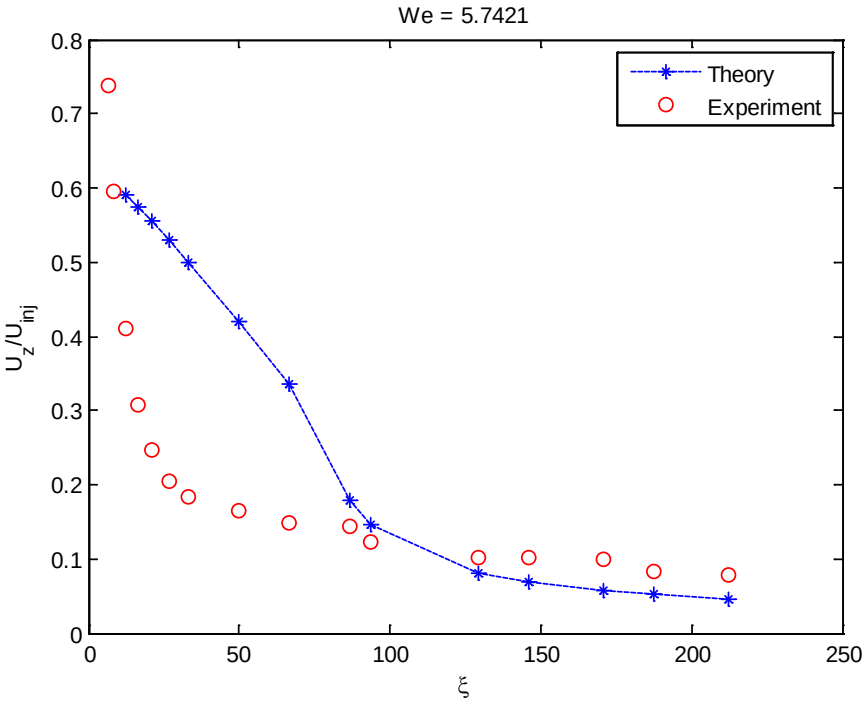

Fig. 24. Axial Variation of Axial Droplet Velocity. Plot of the droplet axial velocity at various axial location for We = 5.7421.

While no other velocity components were given from experimental measurements, it is still interesting to see the behavior of all the components of the liquid and gaseous velocity (see fig. 25-29.). It is clear that all the velocities, regardless of the initial injection velocity, converge to the same value at far downstream locations. This behavior is exactly replicated in experiment (Saha et al.). Another aspect that can be seen from the plots is that the entrained velocities are significantly smaller than the droplet velocity which validates the droplet-driven assumption of the model. Furthermore, the droplet tangential velocity is almost negligible, therefore, not including the tangential velocities of the gas should not affect the model noticeably. One final important concept that can be observed from these results is that the velocity scale, U_{inj}, was the correct scale to be used because when all the non-dimensional forms are plotted together, they all

converge to the same line (see fig. 30-31.). Finally, it should be restated that while the comparison with the experiments of Saha *et al.* help clarify some general behavior of the solutions, they should not be compared exactly as the data presented in the experiment is different than what the model calculates. With this in mind, all further studies in this paper will be conducted with the constant value of K = 3.5 that was derived from the Tratnig and Brenn data.

Now that the model has been thoroughly validated, extensive parametric studies will be performed in the next chapter in order to observe the behavior of pressure-swirl atomizers.

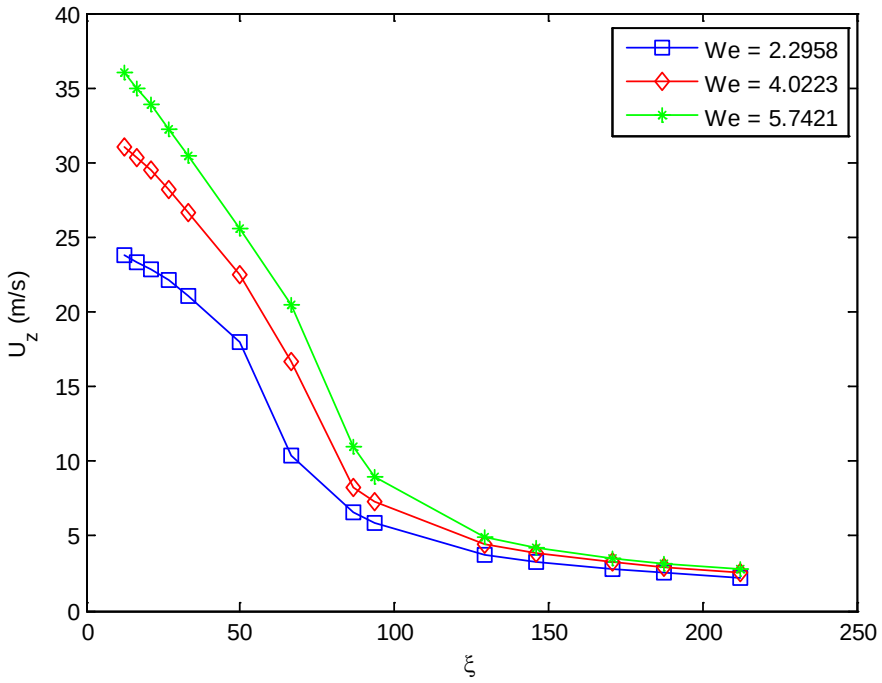

Fig. 25. Dimensional Droplet Axial Velocity. Plot of the droplet axial velocity for all three test cases.

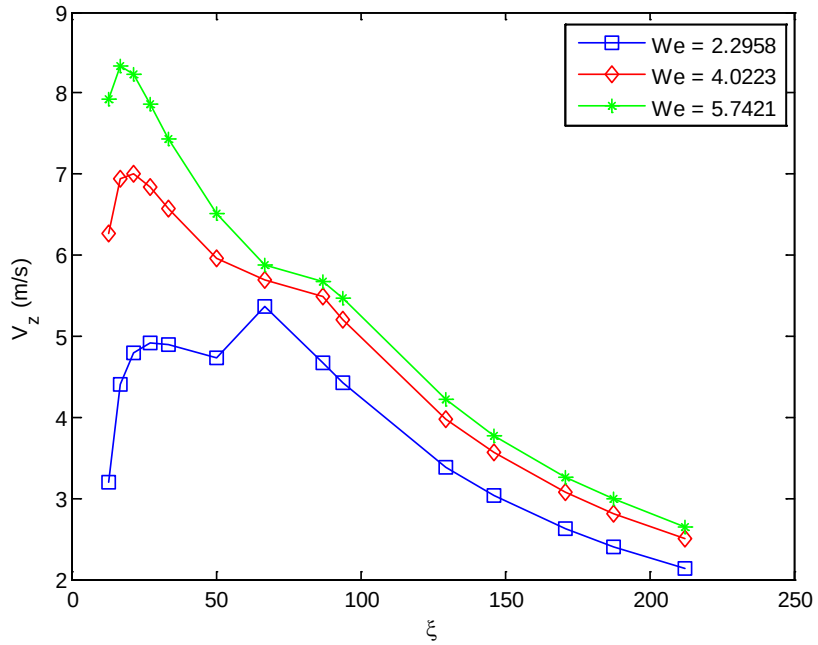

Fig. 26. Dimensional Entrained Axial Velocity. Plot of the entrained axial velocity for all three test cases.

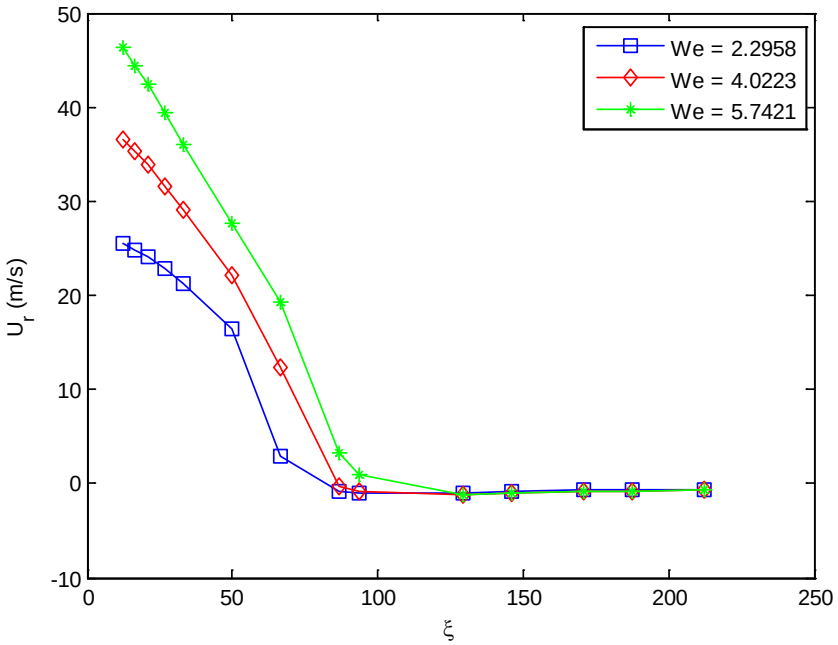

Fig. 27. Dimensional Droplet Radial Velocity. Plot of the droplet radial velocity for all three test cases.

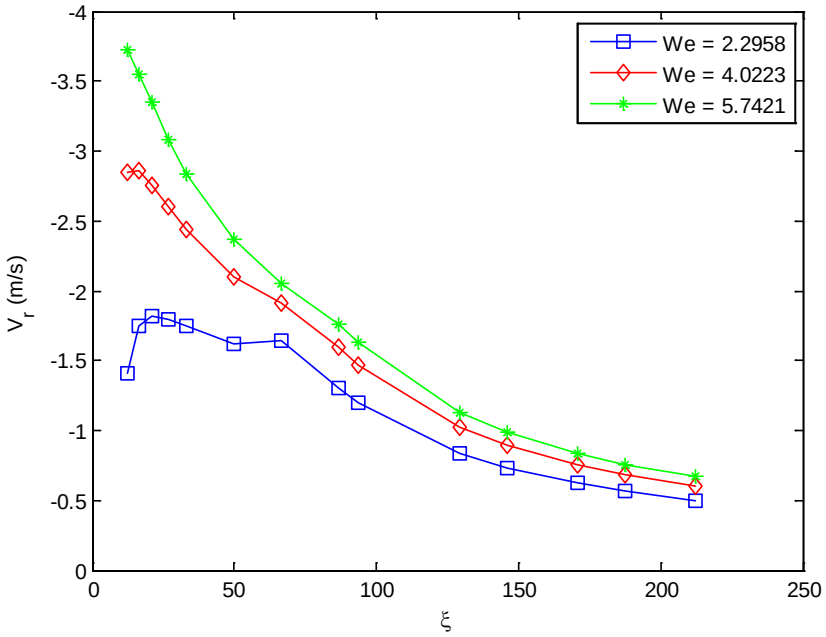

Fig. 28. Dimensional Entrained Radial Velocity. Plot of the entrained radial velocity for all three test cases.

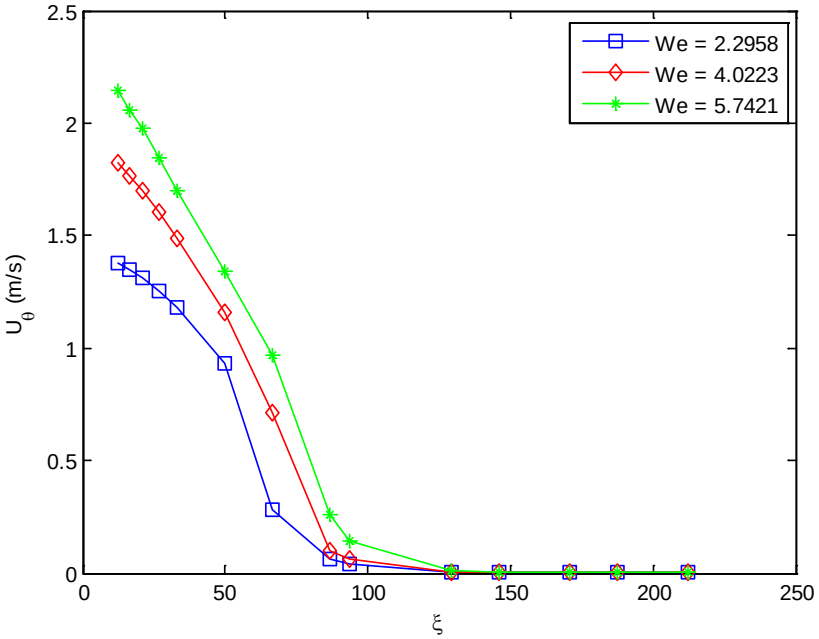

Fig. 29. Dimensional Droplet Tangential Velocity. Plot of the droplet tangential velocity for all three test cases.

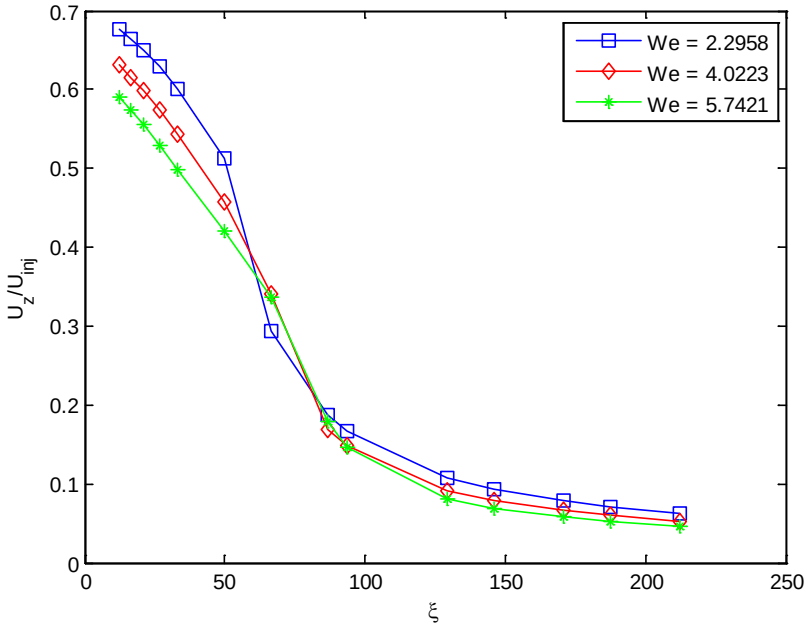

Fig. 30. Droplet Dimensionless Axial Velocity. Plot shows that the injector velocity was the correct velocity scale.

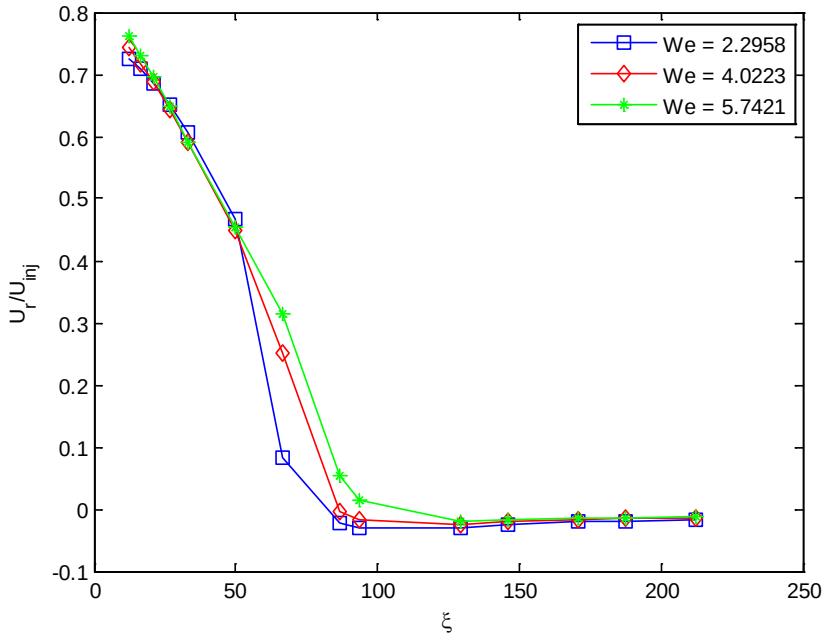

Fig. 31. Droplet Dimensionless Radial Velocity. Plot shows that the injector velocity was the correct velocity scale.

CHAPTER 4

PARAMETRIC STUDIES

I. Parametric Studies:

For the first parametric study, the injection velocity and density ratio will be varied and all other properties kept constant. In reality, the injection velocity should also affect the initial half-cone angle. However, due to the fact that no method has been determined in this study to calculate the initial angle, it will be kept at a constant value of 40°. The liquid and gas will be water and air at standard temperatures, respectively. Since the gas viscosity is mainly a function of temperature, it is a valid assumption to state that it will not change by changing the density ratio. The initial conditions and parameters for this particular study are given below (see table 3.). Please note that the initial sheet thickness had to be determined from the empirical relation given in the 'Model Development' section. The dimensionless axial distance used for this study is 200 injector diameters away from the nozzle. Such a large value for the axial distance was chosen in order to ensure that only the fully atomized values are acquired. The sheet breakup location was assumed to be 2 injector diameters away from the nozzle measured from the center axis, although this may not be the case in reality as the breakup distance is a function of injection properties. Finally, the injector diameter was taken to be 1 mm.

Table 3

Initial conditions for varying injection velocity

$1/\rho^* = 50$			$1/\rho^* = 775$			$1/\rho^* = 1500$		
We	Re	t_0^*	We	Re	t_0^*	We	Re	t_0^*
18.320	2.402E+05	0.3409	1.182	2.402E+05	0.3409	0.611	2.402E+05	0.3409
58.162	3.813E+05	0.2706	3.752	3.813E+05	0.2706	1.939	3.813E+05	0.2706
114.321	4.996E+05	0.2364	7.376	4.996E+05	0.2364	3.811	4.996E+05	0.2364
184.653	6.053E+05	0.2148	11.913	6.053E+05	0.2148	6.155	6.053E+05	0.2148
267.839	7.024E+05	0.1994	17.280	7.024E+05	0.1994	8.928	7.024E+05	0.1994
362.946	7.931E+05	0.1876	23.416	7.931E+05	0.1876	12.098	7.931E+05	0.1876

The distribution of SMD with respect to the injection velocity can be seen in fig. 32. It is evident that the SMD drops rapidly with increasing injection velocity. This behavior is common to all classes of injectors. The rate at which the SMD decreases is very high initially, but it seems that the values tend to level off for very high injection velocities. Realistically, as the injection velocity is increased to even higher values, the flow will become highly turbulent and contain recirculation zones that will alter the behavior drastically. Based on this reasoning, it is not advisable to utilize this model for higher injection velocities without accounting for the proper physics.

Another interesting aspect that can be observed from fig. 32 is that as the gas density is increased (low $1/\rho^*$), the SMD is drastically reduced. This can be attributed to the fact that with higher gas densities, the interaction between the droplets and the air is much higher, therefore the air performs more work on the droplets and breaks the liquid apart. One thing that should be noted is that with increasing gas densities, the assumptions made in regards to the liquid not losing too much of its kinetic energy in the primary atomization regime becomes less valid. In such high pressure situations (keeping

temperature constant), the model may need to be adjusted to account for such losses. As mentioned previously, this shouldn't pose too great of a difficulty, if the proper boundary-layer methods are applied. Another aspect that is affected by high gas pressure is that the cone angle will not remain constant across the entire spray volume. It has been noted that the conical spray tends to contract further downstream due to the aerodynamic drag pulling the droplets towards the center axis (Rothe and Block). Extending the model to account for this should not be difficult since the velocity history is already known and can be used to determine how far the droplets have moved inwards based on the radial component.

It is important to also observe the velocity distribution of the droplets and the air by varying the gas density (see fig. 33-34.). It's clear that the axial droplet velocity dies out very rapidly as the ambient pressure is increased, whereas the axial air velocity is not very affected by the density ratio. This insensitivity to the density ratio can be seen by observing the equation for the axial air velocity. It shows that the density ratio is not a direct parameter in the equation and only comes in indirectly via the Reynolds number.

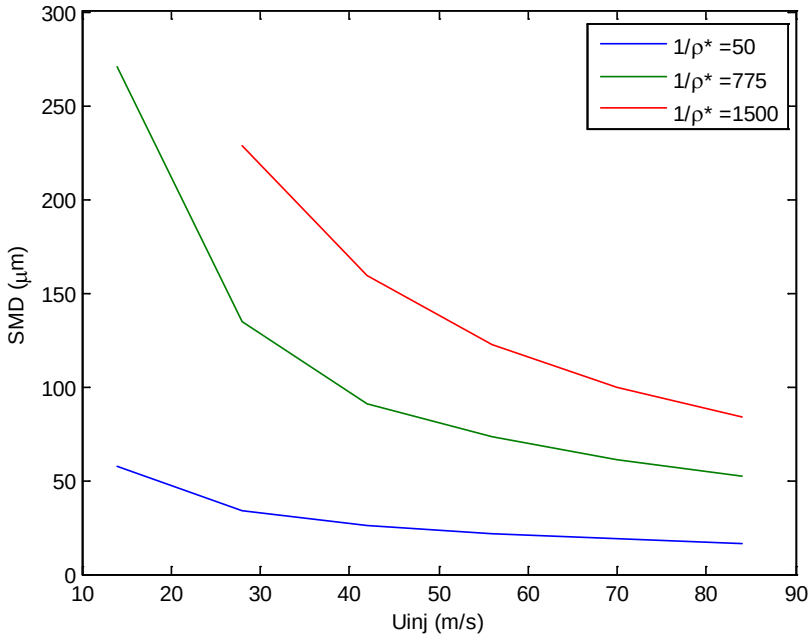

Fig. 32. SMD Variation With Injection Velocity. Plot depicts how the SMD varying with injection velocity and density ratio.

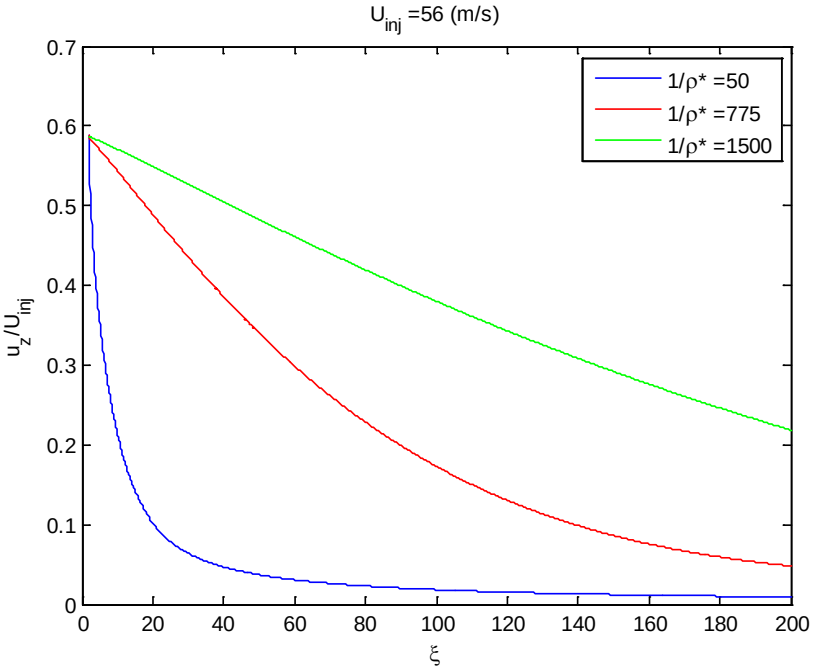

Fig. 33. Dimensionless Axial Velocity With Varying Gas Density. Plot depicts how the axial droplet velocity changes with changes to the ambient conditions.

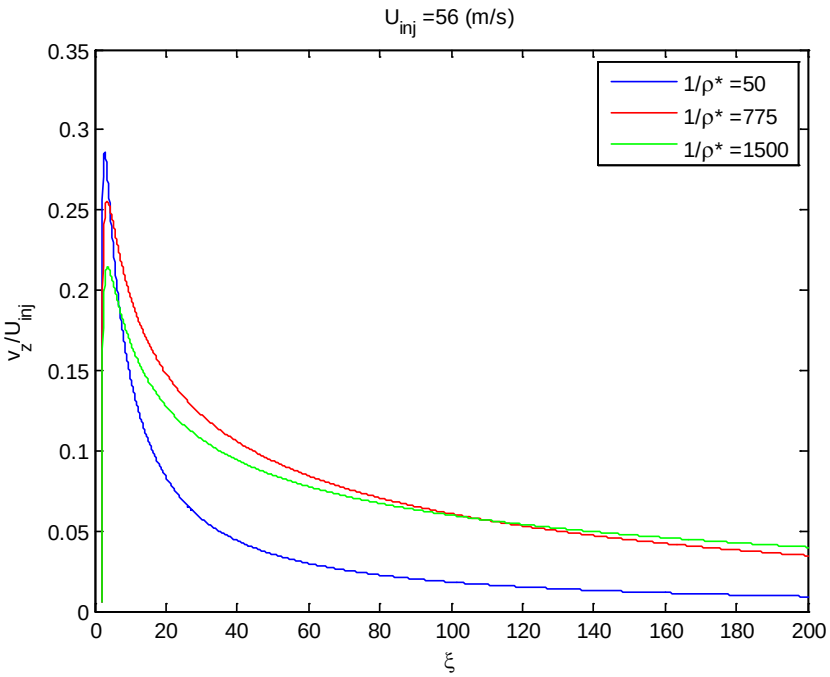

Fig. 34. Entrained Axial Velocity With Varying Gas Density. Plot depicts how the entrained axial velocity changes with changes to the ambient conditions.

Another aspect of pressure-swirl atomizers that is important to understand is how the injector performs at different axial distances. This can be critical in combustion applications where space is limited and the atomizer needs to perform well at very short distances. A simulation was conducted from 80 to 450 injector diameters from the orifice. A large enough distance was chosen as the starting point in order to ensure that all aspects of primary and secondary atomization were completed and all the liquid was in spherical form. In addition to the axial distance, three different injector diameters were used in order to determine its effect on the spray quality. All other injector parameters were kept constant. An injection velocity of 49 m/s was used as well as an initial cone angle of 40°. Water and air at standard conditions were used for the liquid and gas phases. All the necessary initial conditions are given in table 4.

Table 4

Initial conditions for varying injection diameter

D_{inj} (mm)	0.5	1	2
We	5.616	8.916	14.153
Re	3.4882E+05	5.5371E+05	8.7897E+05
t_0^*	0.2829	0.2245	0.1782

The plot for the Sauter mean diameter is given in fig. 35. It is clear that the SMD rapidly drops at downstream locations from the nozzle until it converges to a final value. This was seen in the previous validation section. The SMD also tends to increase noticeably with increasing injector diameter. This behavior is expected because the larger the injector orifice is, the larger the initial sheet thickness will be, and as mentioned in previous chapters, the SMD for pressure-swirl atomizers tends to scale with the initial sheet thickness. This is in contrast to plain-orifice atomizers where they tend to scale better with the injector diameter. For a full understanding of this relationship, it behooves to inspect the non-dimensionless forms of the Sauter mean diameter. The SMD was scaled with respect to the injector diameter and the initial sheet thickness (see fig. 36-37.). It is interesting to see that the non-dimensional forms of the SMD behave opposite to what was just witnessed in that they decrease with increasing injector diameter. Also, it is evident that the SMD scales in a much preferable fashion with respect to the initial sheet thickness than the injector diameter, confirming experimental observations. This is due to the fact that SMD^* values have the same order of magnitude for different injector diameters, whereas in the case of SMD/D_{inj}, it changes quite drastically. The velocity

distributions for each case is also given in fig. 38-39. It's discernable that while initially the velocity distributions are different for different injector diameters, they all converge to the same final value. This behavior is confirmed in experiment (Saha et al).

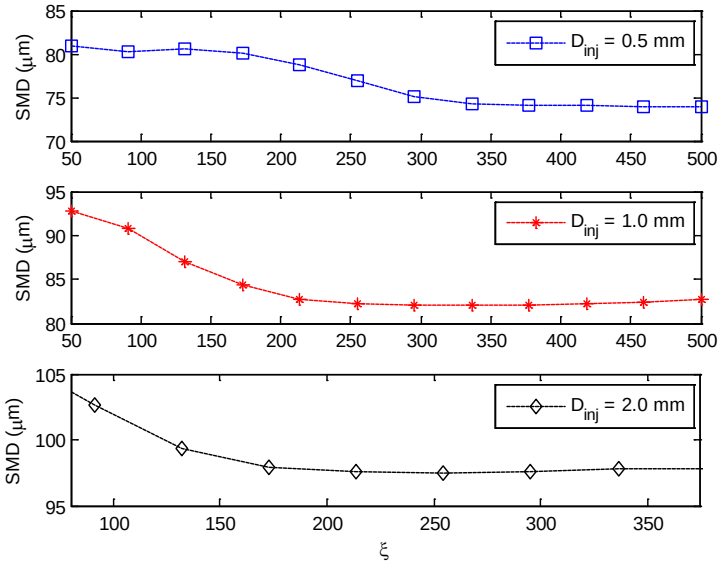

Fig. 35. Axial Variation of SMD For Different Injection Diameters.

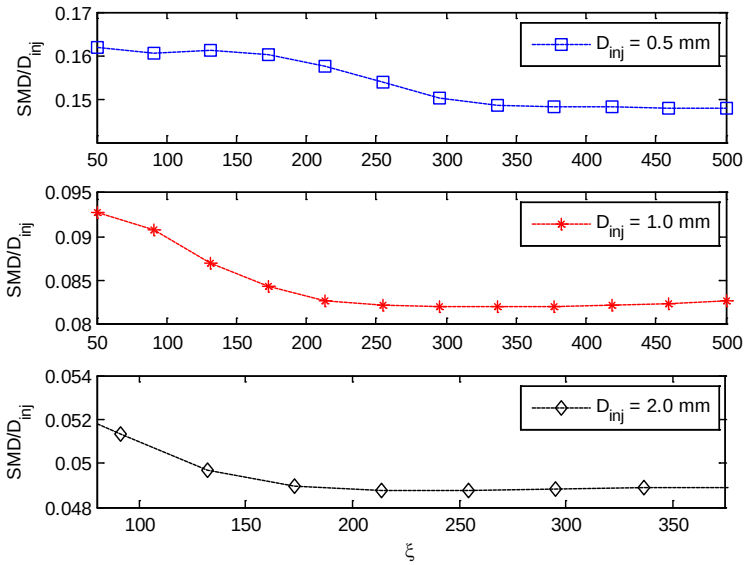

Fig. 36. SMD Non-dimensionalized With Injection Diameter.

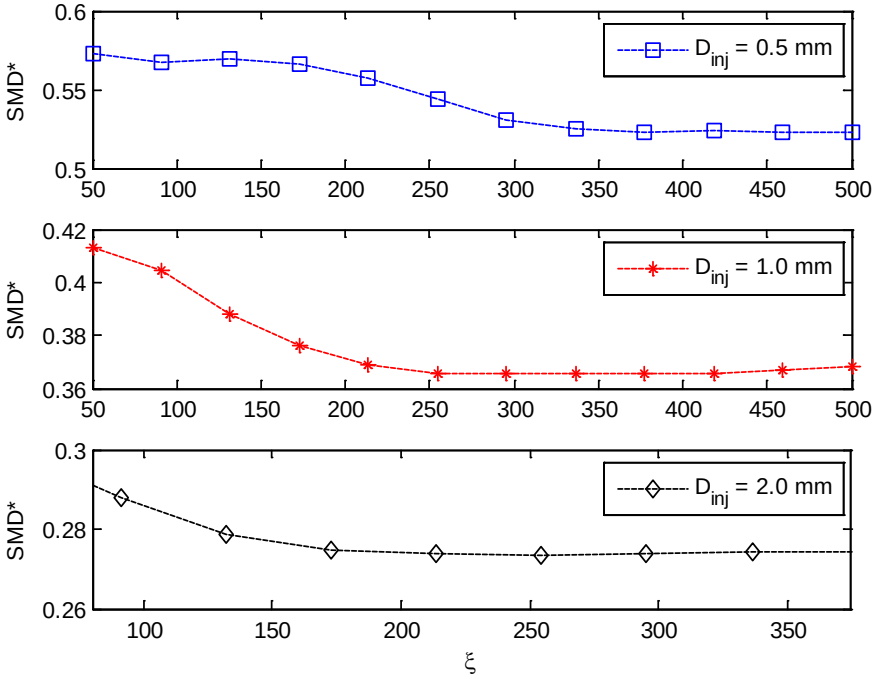

Fig. 37. SMD Non-dimensionalized With Initial Sheet Thickness.

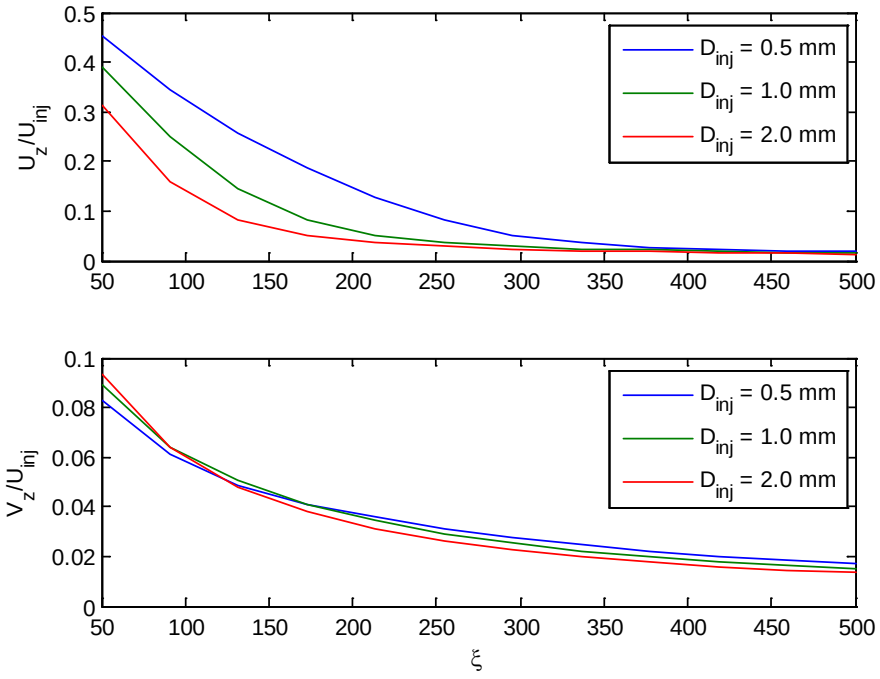

Fig. 38. Droplet and Entrained Axial Velocity For Different Injection Diameters.

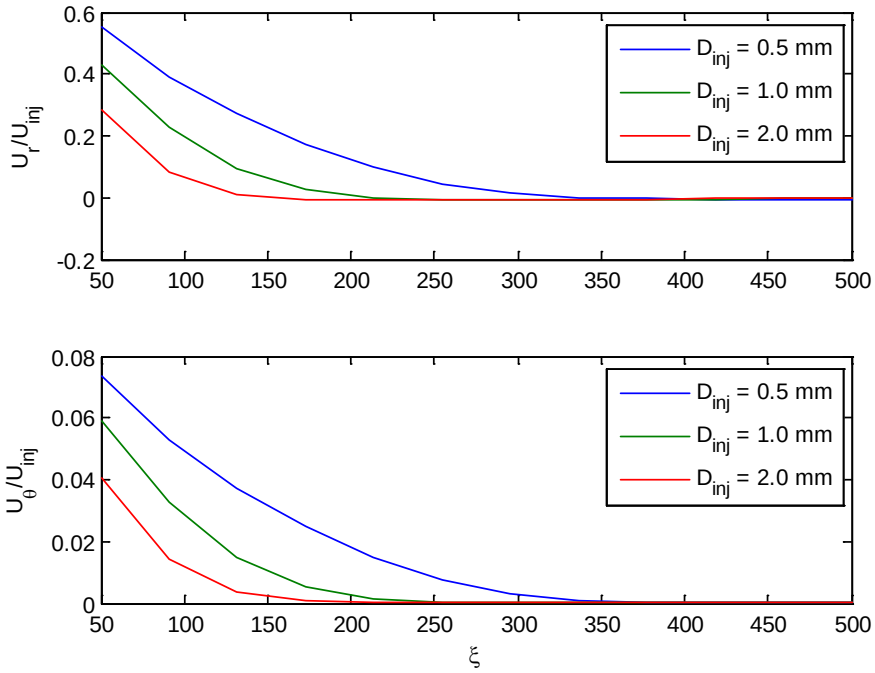

Fig. 39. Droplet Radial and Tangential Velocity for Different Injection Diameters.

Another important factor in the atomization process is the effect of surface tension. In general, surface tension as well as viscosity varies with temperature, therefore the surface tension cannot be altered on its own without affecting other liquid properties. With that in mind, for this initial parametric study, a *theoretical* liquid will be used that has the property of constant viscosity with respect to temperature. This is only to get a feel for the effects of surface tension. A more practical parametric study will be done where the liquid viscosity changes with the surface tension. It should be noted that since no account has been for the internal structure of the liquid sheet or droplets, the liquid viscosity does not affect the equations directly. The only place it appears is in the determination of the initial sheet thickness based on the empirical formula given in previous sections. That said, as previously mentioned, the final SMD values scale

noticeable with the sheet thickness. Consequently, a more practical study accounting for the changes in liquid viscosity is warranted. For this study, the gaseous medium will be at standard conditions. The injection velocity will be 49 m/s with a cone angle of 40 degrees. Since the liquid density does not change drastically with the temperature ranges considered (0-90° Celsius), it will be kept at a constant 998 kg/m^3. The injector diameter used will be 1 mm. All SMD values are determined for an axial location equal to 200 injector diameters. The initial conditions for this parametric study are given in table 5.

Table 5

Initial conditions for varying surface tension

We	Re	t_0^*
8.586	5.5371 E+05	0.2245
10.602	5.5371 E+05	0.2245
13.858	5.5371 E+05	0.2245
19.996	5.5371 E+05	0.2245
35.901	5.5371 E+05	0.2245
175.428	5.5371 E+05	0.2245

The effect of the surface tension on the SMD can be seen in fig. 40. The behavior of the plot is as expect in the sense that the SMD decreases linearly with decreasing surface tension, but the change is almost indistinguishable. In the SMD equation developed earlier based on the conservation energy, the only location the surface tension appears is in the surface tension energy term. This plot indicates that this energy

component is significantly smaller than other terms such as the kinetic energy. Due to this reason, it is constructive to simulate the atomization process for smaller injection velocities. The reasoning here is that if the kinetic energy is comparable to the surface tension energy, then there should a perceivable change due to any alteration to the surface tension. Observing fig. 41-42, it is unquestionable that this is indeed the case. It seems that at the lowest velocities, the surface tension has a dramatic effect.

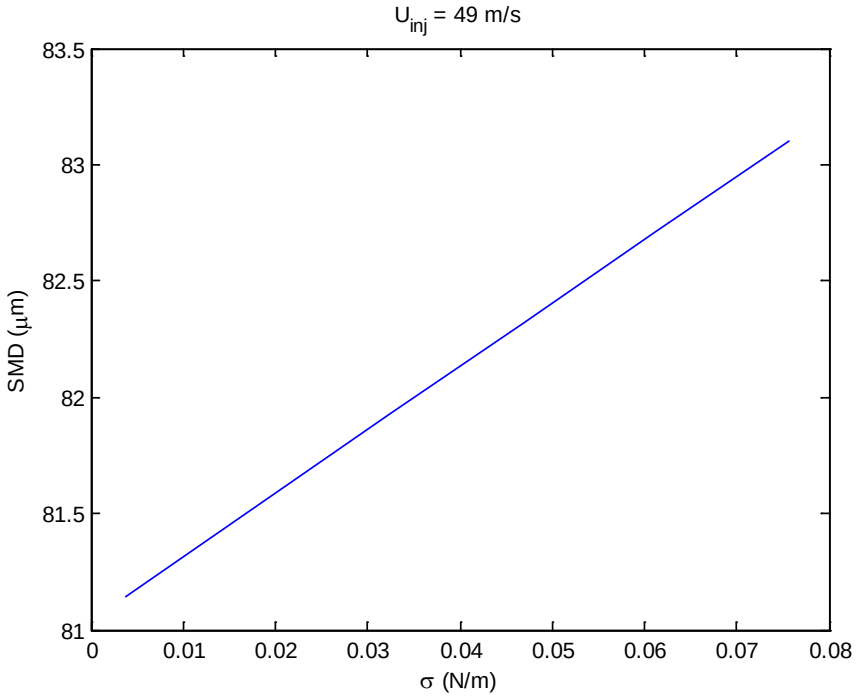

Fig. 40. Surface Tension Effects On Droplet Diameter. Plot depicts surface tension effects on the droplet diameter at high injection velocities.

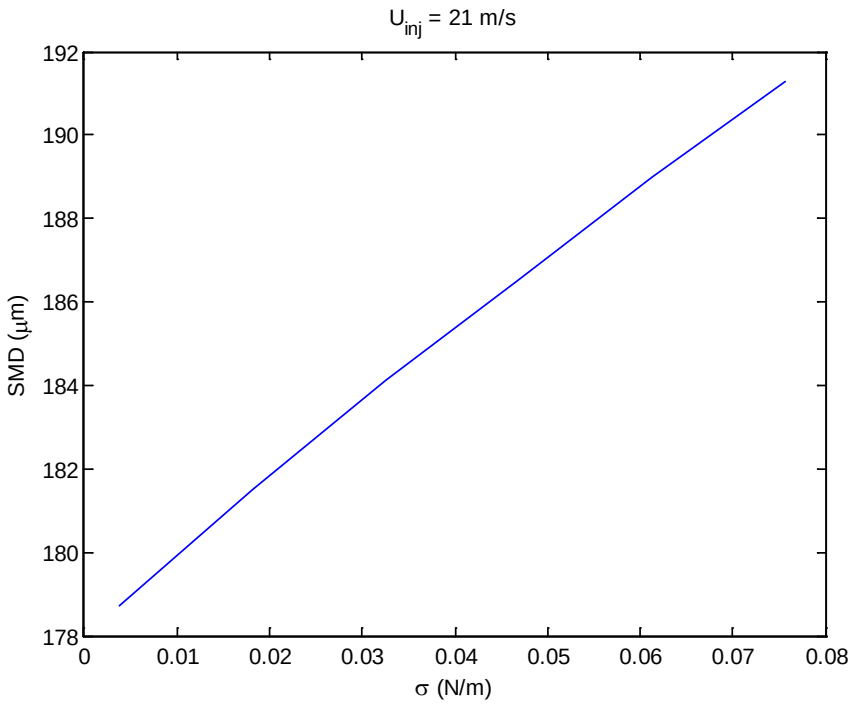

Fig. 41. SMD Variation With Respect To Surface Tension. Plot depicts surface tension effects on the droplet diameter at medium injection velocities.

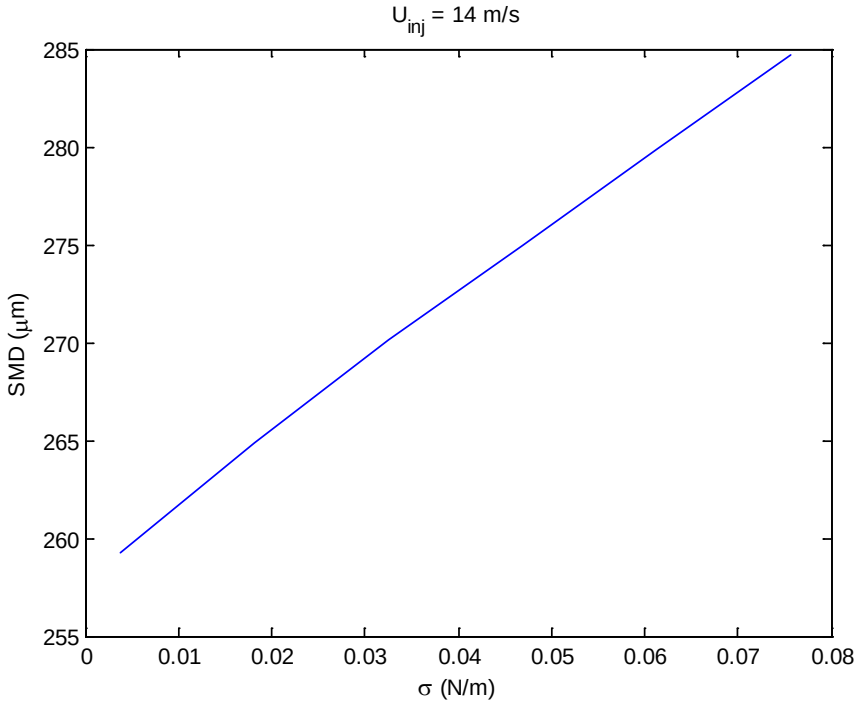

Fig. 42. SMD Variation With Respect To Surface Tension. Plot depicts surface tension effects on the droplet diameter at low injection velocities.

From an energy perspective, due to the fact that most modern pressure-swirl atomizers operate at extremely high injection velocities, the effects of surface tension will not be very discernable and concentration should be placed more on other parameters in order to change the atomization quality. It should be noted that the cone angle was kept constant for these three simulations whereas, in reality, the cone angle should drop drastically with decrease in the injection velocity. Aside from its contributions to the SMD, the surface tension also appears in the thin-sheet dynamic equations developed earlier. The behavior is the same in the sense that at very high injection velocities, the surface tension effects are almost negligible due to the fact that it cannot overcome the sheet expansion that is the result of the centrifugal terms.

This particular analysis, while beneficial in the sense that it revealed the effect of surface tension, is not very practical. As discussed earlier, surface tension is a function of temperature as is the viscosity, and one cannot be altered without influencing the other. A more practical simulation would be to alter both of these terms accordingly. For this next calculation, water will be simulated from 0-90° Celsius. All other conditions will be kept constant as before. Its properties and initial conditions can be found in Table 6. The plot for this simulation is given below in fig. 43. While the general behavior is the same as before, when liquid viscosity is allowed to be changed, the slope of the SMD with respect to the surface tension changes. It is critical to point out again that the liquid viscosity only plays an indirect role in the present model. The major role of liquid viscosity is during the instability mechanisms of the primary atomization regime. If this is accounted for, there should be a much more noticeable change in the solutions.

Table 6

Initial conditions for varying surface tension and liquid viscosity

σ (N/m)	**μ_L (mPa-s)**	**We**	**Re**	**t_0^***
0.0756	1.787	2.537	3.817 E+05	0.3612
0.0742	1.307	2.329	3.439 E+05	0.3254
0.0712	0.798	2.059	2.918 E+05	0.2760
0.0679	0.547	1.903	2.572 E+05	0.2434
0.0644	0.404	1.814	2.325 E+05	0.2200
0.0608	0.315	1.768	2.140 E+05	0.2025

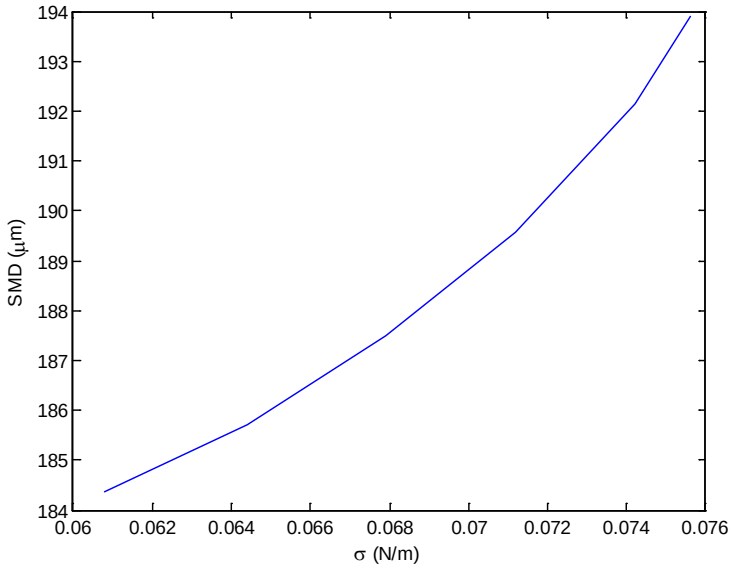

Fig. 43. SMD Variation with Surface Tension and Liquid Viscosity.

Another important study that can be made is to see how the SMD varies with respect to the Weber number. This can be seen in fig. 44. It is obvious that as the Weber

number is increased, the SMD drops quite rapidly. The change in the SMD is drastic at lower Weber numbers, but it becomes less important at very high Weber numbers.

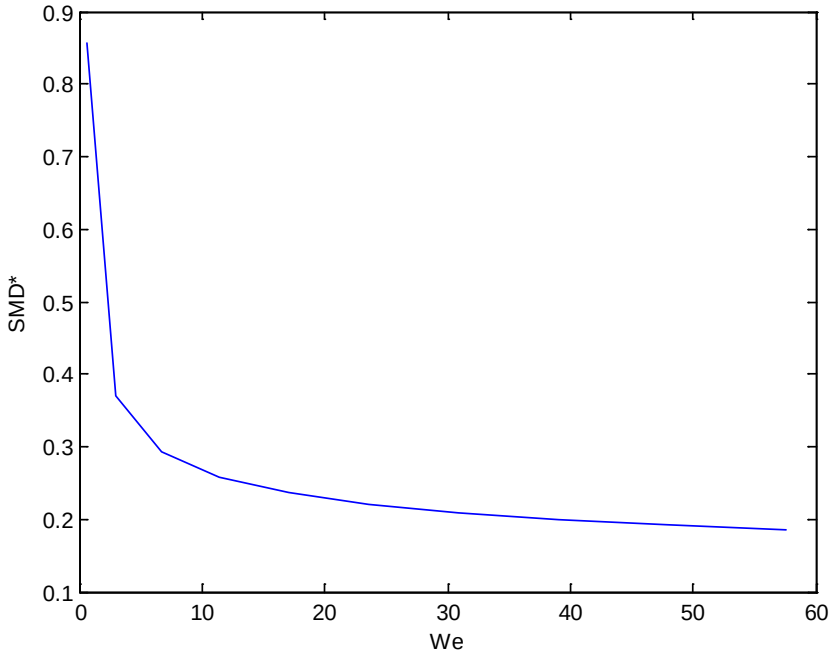

Fig. 44. SMD* Variation With Respect To Weber Number.

The Weber number is not the only factor that can affect the SMD in pressure-swirl atomizers. Another important parameter is the density ratio between the liquid and gas phase. It is known that at higher gas densities, there should be greater aerodynamic drag that acts on the droplets. This higher exchange of momentum can significantly reduce the droplet sizes. This is clearly depicted in fig. 45. The results of the present theoretical model should become less and less accurate at extremely high gas densities due to the fact that the contraction of the spray is not accounted for. Since the velocity profile is already being calculated, this should be easily remedied in future works.

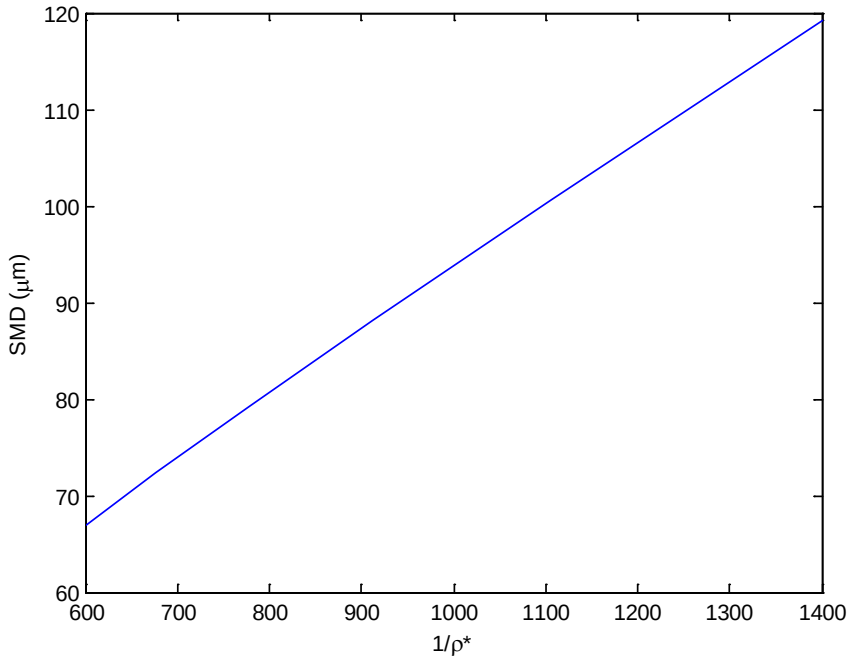

Fig. 45. SMD Variation With Respect To Density Ratio.

Since the sheet breakup length is an experimental input in the present theoretical model, it's important to see its effects on the overall solution. Considering fig. 46, it's evident that the sheet breakup length can have a significant effect on the final SMD value. Finally, the cone angle was varied in the calculations in order to determine how the spray angle changes the SMD (see fig. 47.). In general, the cone angle varies drastically with operating conditions; however, for the present calculations all other conditions were kept the same. Since the initial axial and swirl velocities are calculated by Eq. 37 and 38, respectively, changing the cone angle effectively alters their ratio at the injector. From fig. 47, it seems that the SMD increases with increasing cone angle. This seems counter intuitive as droplets have a tendency to decrease in size at higher cone angle. This discrepancy may have come from the fact that the cone angle should generally be a

function of operating conditions and in these calculations everything besides the cone angle was kept constant. With this said, it is important to perform further investigations in order to understand whether this is a source of error within the theoretical model.

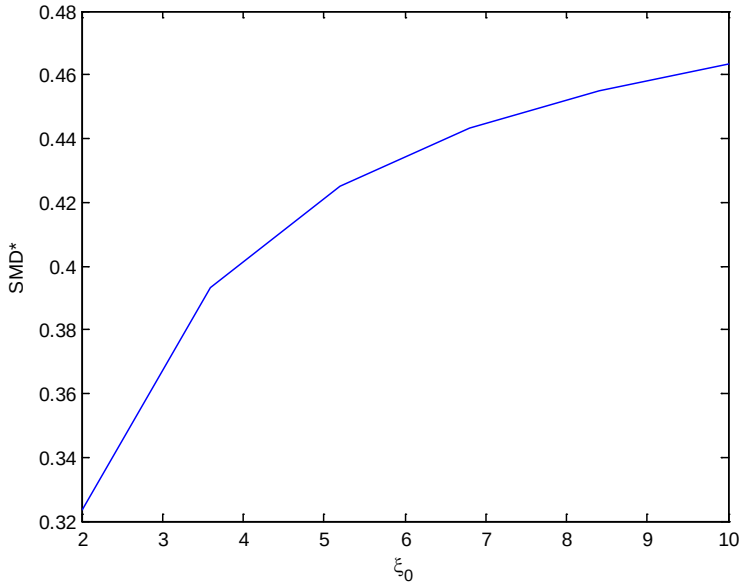

Fig. 46. SMD* Variation With Respect To Sheet Breakup Length.

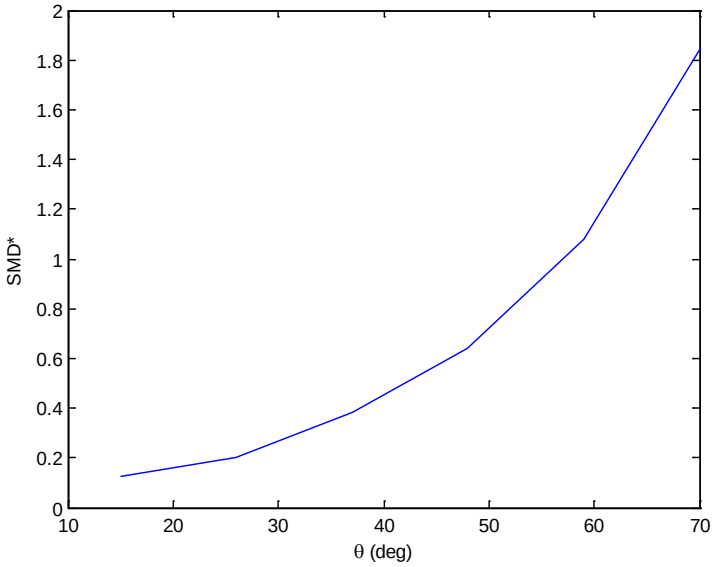

Fig. 47. SMD* Variation With Respect To Spray Cone Angle.

CHAPTER 5

CONCLUSIONS

I. Extension of Model and Future Improvements:

The model developed in this thesis was extensively validated in the previous chapters and found to be quite versatile in correctly determining the atomized Sauter mean diameter of the droplets as well as their velocity history throughout the atomization process of pressure-swirl injectors. Through this validation procedure it was also found that the model had a few shortcomings, namely that it performed poorly at very lone cone angles and Weber numbers. In addition, the model made no account of turbulence, hydrodynamic instabilities, contracting cone angle at higher gas densities, the kinetic energy loss of the primary atomization regime, unsteady drag coefficient relation, or any drop-drop interactions. In this section, these shortcomings will be discussed in detail in order ascertain how they may be improved upon in future works.

One of the main aspects of atomization is that the liquid-gas interaction can become highly turbulent for certain flow conditions. While the main source of turbulence is due to the droplet-air interaction, pressure fluctuations in the injector can also be a source of turbulence. The presence of turbulence effectively adds to the droplets kinetic energy due to the fluctuating turbulent velocities. Unfortunately, including the effects of turbulence in the present model will be extremely difficult from first principles. In general, the most feasible and practical method would be to include different turbulence models to account for this. Numerous previous authors have attempted to include turbulence effects by utilizing turbulence models developed for single-phase jets. While they have met some limited success, this method should not be done without careful

consideration as the underlying physics may be too different to apply such models correctly. This is especially critical when using constant parameters that have been fine tuned for single-phase jets. It is this author's opinion that it is better not to account for turbulence and be valid in a limited range of operating conditions than to account for it and be uncertain about its validity. If accounting for turbulence, it is critical to note that the viscous dissipation term has to be altered as the general analysis was performed for a laminar boundary layer. The effect of turbulence in the boundary layer makes the problem significantly more complex and, in general, reliance must be made upon experimental observations or numerical calculations. Since the main purpose of the present thesis is to avoid such things as much as possible, it was decided to not include such effects.

In addition to turbulence, this model has made no account for the Kelvin-Helmholtz or Rayleigh-Taylor instability mechanisms that are present in the primary atomization as well as secondary atomization regimes. There is a wall of previous research done in these fields and it should not be too difficult to incorporate such physics into the problem. One of the main benefits of such an analysis would be to determine the sheet breakup length that is used in the model. Having this value would remove one of the dependencies on experimental observation. In addition, instability mechanisms will provide the instantaneous sheet thickness until the point of breakup. Currently, the model is only calculating average values. The reason it was chosen not to include previous works in hydrodynamic instability by Dombrowski and Johns was that their analysis has a tendency to over predict the breakup length, which can affect the total kinetic energy loss, work, and dissipation terms in the model (Tratnig and Brenn). In addition to

calculating the sheet breakup length, hydrodynamic instability analysis will allow for the *direct* introduction of the liquid viscosity in the model equations. Currently, the model is very weakly dependent upon the liquid viscosity through the empirical relation given for the initial sheet thickness. If the mass flow rate is given, then the empirical equation is not even used, and the liquid viscosity has no contribution to the model in any fashion.

Another aspect of the primary atomization regime in the model that stands to be improved upon is the calculation of the velocity drop across the sheet portion of the spray. As discussed previously, this can be done via boundary layer methods. While, in general, three component boundary layer assessment is very difficult, Pohlhausen's momentum integral approximation method may be used to get a first-order assessment of this velocity loss. If this calculation is included, it would remove the discontinuity in the energy equation at $z = Z_0$. It stands to reason that the final atomized droplet diameters would also be affected by this calculation. It should be noted that if turbulence is to be accounted for, this boundary layer analysis may not work as well and other methods may have to be used. This extension of the model should not pose too great of a difficulty and should be attempted first in order to improve the calculations.

One of the weakest aspects of this model is in determining the initial cone angle of the spray as well as the initial swirl component of the velocity. As it stands, the cone angle is taken directly from experimental measurements which are generally given as some average value across the *entire* sheet portion. A more direct calculation seems feasible through conservation of energy and angular momentum analysis across the injector orifice. Unfortunately, all current attempts to include such a calculation in this thesis led to failure. The initial swirl component calculation is also in need of

improvement. In general, experiments do not provide the necessary initial conditions needed to make the correct calculation. The swirl component at the injector orifice should be a function of the internal geometry of the atomizer as well as the injection pressure. Lacking such information, the initial tangential velocity had to be calculated from

$$U_{\theta-inj} = U_{inj} \sin\theta_0$$

This is based on previous bodies of work, where it was assumed that if the injector diameter is sufficiently small, the radial component of velocity will be small. And from geometrical considerations, the axial component of velocity is

$$U_{z-inj} = U_{inj} \cos\theta_0$$

And if the total velocity is equal to

$$U_{inj}^2 = U_{z-inj}^2 + U_{\theta-inj}^2$$

Then it is obvious that the initial swirl component has to be of the form given above. Although this is slightly inaccurate, the overall effect on the solution is minimal as the swirl component dies out quite rapidly due to conservation of angular momentum and the rapid sheet expansion.

Previous experiments have shown that for high gas densities, the spray cone angle does not remain constant as the droplets traverse downstream. At sufficiently far enough locations, the spray cone will begin to contract due to the aerodynamic forces carrying the droplets towards the center. As the gas density is increased, this effect becomes more pronounced until the spray becomes very dense. This contraction should be easily accounted for in the present model due to the fact that the velocity history is already being calculated. Knowing the radial component of the droplet and air velocities, it is

simple to figure out how far the droplets are displaced radially as they travel downstream. This was not included in this thesis due to the lack of time, but future works should include this effect for the complete picture of the atomization process.

The aerodynamic drag force being calculated was determined by a drag coefficient derived from empirical observations of a single sphere in a steady flow. In general, atomization sprays contain a myriad of droplets that form in various groups that prevents the drag equation from being directly applicable. In addition, the droplets are constantly accelerating; consequently, the steady drag coefficient is not exactly valid. The assumption made here was that the droplets relaxation time is fast enough where any unsteady behavior does not matter. Finally, due to numerical reasons, a drag coefficient was used that was valid for droplet $Re \leq 1000$. If operation conditions dictate such that the droplet Reynolds numbers become larger than 1000, then it will be necessary to utilize a different equation. With that said, the majority of droplets will be well below such values and the equation used should be sufficient.

The current method of determining the viscous dissipation term in the energy equation is based on an order of magnitude analysis, and so it requires a constant parameter that had to be tuned to experimental observations. While this constant parameter seems to work for a variety of operating conditions, it is of paramount importance that a more detailed assessment of the boundary layer dissipation be made that is consistent with the model. Such analysis will aid in removing the dependencies of the constant parameter and allow for a full calculation without the need to resort to experiment. Failing such considerations, the viscous dissipation model can still be improved upon for a much more accurate solution. Currently, the model assumes that the

volume over which the dissipation is occurring per droplet is proportional to its surface area times the boundary layer length. This is not always the case and may lead to errors under certain conditions.

It was also observed that the present model does not account for any drop-drop interactions or coalescence. While this is not really an issue for the majority of the spray, it can present problems at far downstream locations where the coalescence and droplet collision probabilities increase quite rapidly. The overall effect of the drop-drop interactions is to increase the droplet diameters after atomization has been fully completed. While the increase in size is noticeable, it is not of such significance as to completely invalidate the solution at very far axial locations. With that said, accounting for such behavior will allow for a much more complete picture of pressure-swirl atomizers.

Finally, since mass and heat transfer are of paramount importance in the atomization process especially in combustion applications, including such effects would be of great benefit for practical purposes. While such analyses is beyond the scope of this study, significant work has been done in the past and may be included in the model developed thus far (Lee and Tankin, “Stud. Liq. Spray Cond.”).

II. Conclusions:

In this study, a highly physics-based model was developed in order to calculate the Sauter mean diameter of pressure-swirl atomizers via the conservation of energy. In addition, the droplet and entrained air velocity histories were determined through integral momentum and continuity methods. A viscous dissipation model was also derived in

order to account for the dissipation that occurs between the droplet and the air. While the main goal of this thesis was to minimize dependencies on empirical observations, the viscous dissipation model was based on an order-of-magnitude boundary-layer analysis and required a constant parameter that had to be tuned through experiment. This constant parameter showed to be valid for a wide range of operating conditions and did not need any further fine tuning.

The model developed was extensively validated through numerous independent experiments and a detailed assessment of its shortcomings was made. It was found that the model performed poorly for very low injection velocities, or Weber numbers, and for very small cone angles. In addition to the validation process, extensive parametric studies were performed in order to understand the behavior of simplex atomizers. It was found that the sheet thickness is a major contributing factor towards the final SMD values. It was also discovered that for very high injection velocities, the surface tension does not contribute significantly to the final solution. Since this is the main operating range for most modern pressure-swirl atomizers, it is beneficial to alter other parameters to increase the injector's performance. Finally, it was shown that the gas density plays a major role in the atomization process in that as the density is increased, the droplet diameters are also rapidly reduced. Increasing the gas density reduces the spray angle and penetration which can alter the spray control necessary in certain combustion processes, and therefore, a compromise should be found.

Since pressure-swirl atomizers are major component in many combustion applications, the need for a sound model is paramount. While CFD simulation and experimental observation reveal more detailed physics, they are limited by the time and

cost required to conduct them. Having a model that can give a good first-order approximation for the SMD is critical for initial parametric studies in order to determine what atomizer parameters need to be changed for optimal performance. In addition, this model can be used to provide reasonable initial conditions for various combustion CFD applications. As discussed previously, future work can significantly improve the accuracy of this model by including effects such as hydrodynamic instability mechanisms, spray cone contraction, turbulence, and droplet-droplet interactions. Such improvements will aid in creating a robust and physically sound model for the prediction of pressure-swirl atomizer performance.

REFERENCES

Bark, Fritz H., et al. "Swirling Water Bells." *Journal of Fluid Mechanics* 90 (1979): 625-639.

Batchelor, George Keith. *An Introduction To Fluid Dynamics*. New Delhi: Cambridge University Press India, 2009. Print.

Binnie, A. M. and D. P. Harris. "The Application of Boundary-Layer Theory To Swirling Liquid Flow Through A Nozzle." *Quarterly Journal of Mechanics and Applied Mathematics* III.1 (1950): 89-106. Print.

Brena de la Rosa, A., G. Wang and W. D. Bachalo. "The Effects of Swirl on the Velocity and Turbulence Fields of a Liquid Spray." *Journal of Engineering for Gas Turbines and Power* 114 (1992): 72-81.

Cossali, G. E. "An integral model for gas entrainment into full cone sprays." *Journal of Fluid Mechanics* 439 (2001): 353-366.

Dombrowski, N. and W. R. Johns. "The aerodynamic instability and disintegration of viscous liquid sheets." *Chemical Engineering Science* 18 (1963): 203-214.

Ghosh, S. and J. C. R. Hunt. "Induced Air Velocity within Droplet Driven Sprays." *Proceedings of Mathematical and Physical Sciences* 444.1920 (1994): 105-127.

Goldstein, S. *Modern Developments In Fluid Dynamics*. Vol. 1. New York: Dover Publications, 1965.

Gorokhovski, Mikhael and Marcus Herrmann. "Modeling Primary Atomization." *Annual Review of Fluid Mechanics* 40 (2008): 343-366.

Guildenbecher, D. R., C. Lopez-Rivera and P. E. Sojka. "Secondary atomization." *Experimental Fluids* 46 (2009): 371-402.

Herrmann, Marcus. "Detailed Numerical Simulations of the Primary Atomization of a Turbulent Liquid Jet in Crossflow." *Journal of Engineering for Gas Turbines and Power* 132 (2010).

Jiang, Y. J., A. Umemura and C. K. Law. "An Experimental Investigation on The Collision Behaviour of Hydrocarbon Droplets." *Journal of Fluid Mechanics* 234 (1992): 171-190.

Lee, S. Y. and R. S. Tankin. "Study of Liquid Spray (Water) In A Condensable Environment (Steam)." *International Journal of Heat and Mass Transfer* 27.3 (1984): 363-374.

Lee, S. Y. and R. S. Tankin. "Study of Liquid Spray (Water) In A Non-condensable Environment (Air)." *International Journal of Heat and Mass Transfer* 27.3 (1984): 351-361.

Lee, T.-W. and Dan Robinson. "Calculation of The Drop Size Distribution and Velocities From The Integral Form of The Conservation Equations." *Combustion Science and Technology* 183 (2011): 1-14.

Lee, T.-W. and J. Y. Lee. "Momentum Effects On The Spray Drop Size Calculated From The Integral Form of The Conservation Equations." *Combustion Science Technology* 184 (2012): 1-10.

Lefebvre, Arthur Henry. *Atomization and Sprays*. Hemisphere Publishing Corporation, 1989. Print.

Lefebvre, Arthur Henry. "Factors controling gas turbine combustion at high pressure." *Combustion in Advanced Gas Turbine Systems*. Ed. Ian Edward Smith. Oxford: Elsevier, 1968. 221-226.

Lefebvre, Arthur Henry. *Gas Turbine Combustion*. Philadelphia: Taylor & Francis, 1999. Print.

Lefebvre, Arthur Henry. "The Prediction of Sauter Mean Diameter for Simplex Pressure-swirl Atomisers." *Atomisation and Spray Technology* 3 (1987): 37-51. Print.

Lin, S. P. and R. D. Reitz. "Drop and Spray Formation From a Liquid Jet." *Annual Review of Fluid Mechanics* 30 (1998): 85-105.

Mellor, A. M. *Design of Modern Turbine Combustors*. San Diego: Academic Press Inc., 1990. Print.

Park, Hongbok and Stephen D. Heister. "Nonlinear simulation of free surfaces and atomization in pressure swirl atomizers." *Physics of Fluids* 18 (2006).

Parlange, Jean-Yves. "A Theory of Water Bells." *Journal of Fluid Mechanics* 29.2 (1967): 361-372.

Ponstein, J. "Instability of Rotating Cylindrical Jets." *Applied Scientific Research* 8.1 (1959): 425-456.

Prosperi, B., et al. "FPIV study of gas entrainment by a hollow cone spray submitted to variable density." *Experimental Fluids* 43 (2007): 315-327.

Qian, J. and C. K. Law. "Regimes of Coalescence and Separation In Droplet Collision." *Journal of Fluid Mechanics* 331 (1997): 59-80.

Rizk, N. K. and Arthur Henry Lefebvre. "Internal Flow Characteristics of Simplex Swirl Atomizers." *Journal of Propulsion and Power* (1985): 193-199.

Rosenhead, L. *Laminar Boundary Layers*. London: Oxford University Press, 1963.

Rothe, P. H. and J. A. Block. "Aerodynamic Behavior of Liquid Sprays." *International Journal of Multiphase Flow* 3 (1977): 263-272.

Saha, Abhishek, et al. "Breakup and coalescence characteristics of a hollow cone swirling spray." *Physics of Fluids* 24 (2012).

Santolaya, J. L., et al. "Analysis by Droplet Size Classes of the Liquid Flow Structure in a Pressure Swirl Hollow Cone Spray." *Chemical Engineering and Processing* 49 (2010): 125-131.

Schlichting, H. and K. Gersten. *Boundary Layer Theory*. 8th. New York: Springer-Verlag Berlin Heidelberg, 2000.

Taylor, Geoffrey Ingram. "The Dynamics of Thin Sheets of Fluid. I. Water Bells." *Proceedings of the Royal Society of London Series A* 253.1274 (1959): 289-295.

Taylor, Geoffrey Ingram. "The Mechanics of Swirl Atomizers." *Proceedings of The Seventh International Congress of Applied Mechanics*. 1948. 280-285. Document.

Theofanous, T. G. and G. J. Li. "On the physics of aerobreakup." *Physics of Fluids* 20 (2008).

Tratnig, Andreas and Gunter Brenn. "Drop size spectra in sprays from pressure-swirl atomizers." *International Journal of Multiphase Flow* 36 (2010): 349-363.

APPENDIX

Table 1

Tratnig and Brenn initial conditions

Trial	D_{inj} (mm)	μ_L (Pa-s)	We	Re	$1/\rho^*$	t_0^*	S_0^*	Θ_0 (deg)	SMD^*
1	0.762	0.0163	16.641	8.8358E+05	1029.900	0.2633	13.1234	27.50	0.2934
2	0.762	0.0187	21.016	1.0123E+06	1035.714	0.2706	13.1234	25.25	0.2566
3	1.778	0.0121	2.682	3.5360E+05	1013.289	0.1158	6.1867	40.00	0.6343
4	1.778	0.0106	3.861	4.6896E+05	1007.475	0.1432	5.0619	36.00	0.4441
5	0.762	0.0142	18.392	1.1703E+06	1023.256	0.4234	13.1234	30.00	0.1803
6	1.270	0.0132	8.748	8.2156E+05	1018.272	0.2658	10.2362	27.50	0.2744
7	1.778	0.0087	1.872	3.8369E+05	997.508	0.2016	9.5613	31.50	0.4783
8	1.778	0.0403	2.909	3.8119E+05	1059.801	0.1135	12.3735	30.50	0.5582
9	1.778	0.0487	7.666	6.9968E+05	1064.784	0.1437	10.1237	29.50	0.3551
10	1.270	0.0416	14.998	1.0954E+06	1060.631	0.2540	11.8110	25.00	0.2255
11	1.778	0.0529	6.700	7.5986E+05	1067.276	0.1930	13.4983	26.00	0.3233
12	0.762	0.0540	16.791	1.1703E+06	1069.767	0.4243	23.6220	7.50	0.2056
13	1.270	0.0325	8.299	8.5315E+05	1052.326	0.2829	16.5354	24.50	0.2158
14	1.778	0.0468	7.667	8.8024E+05	1063.953	0.2278	17.4353	23.50	0.2470
15	1.778	0.1278	16.150	1.1135E+06	1092.193	0.1642	18.5602	21.50	0.3052
16	1.778	0.1714	15.651	1.0608E+06	1088.040	0.1549	18.5602	21.00	0.2672
17	1.270	0.1400	31.833	1.7344E+06	1091.362	0.2834	18.8976	16.50	0.1716
18	1.778	0.1100	10.369	9.7303E+05	1084.718	0.1980	16.8729	22.50	0.2603
19	1.270	0.1162	20.205	1.4395E+06	1085.548	0.3108	18.1102	12.50	0.2028
20	1.778	0.1018	16.181	1.3492E+06	1083.056	0.2447	16.8729	21.00	0.1860
21	0.762	0.0635	27.295	1.1703E+06	1060.631	0.3720	14.4357	22.50	0.2597
22	1.778	0.0560	7.058	5.2915E+05	1053.987	0.1353	11.8110	27.00	0.4307
23	1.778	0.0578	8.963	6.9968E+05	1058.970	0.1545	9.5613	31.50	0.3251
24	1.270	0.0435	21.561	1.0954E+06	1044.020	0.2525	9.8425	32.00	0.1992
25	1.270	0.0656	26.934	1.3342E+06	1063.123	0.3069	18.1102	19.00	0.1822
26	1.778	0.0521	14.199	9.8055E+05	1038.206	0.2215	12.9359	28.00	0.2006
27	1.778	0.1669	17.874	1.0031E+06	1079.734	0.1670	20.8099	24.00	0.3032
28	1.778	0.1460	17.091	1.0031E+06	1071.429	0.1896	16.8729	23.50	0.2713
29	1.778	0.1576	18.867	1.2037E+06	1071.429	0.2643	16.8729	21.00	0.1889
30	1.016	0.1521	19.631	1.0972E+06	1077.243	0.3298	15.7480	11.50	0.2627